

# A Generalized Approach to Planar Induction Heating Magnetics

by

Richard Yi Zhang

B.E. (Hons), University of Canterbury, New Zealand (2009)

Submitted to the Department of Electrical Engineering and Computer Science

in partial fulfillment of the requirements for the degree of

Master of Science

at the

MASSACHUSETTS INSTITUTE OF TECHNOLOGY

June 2012

© Massachusetts Institute of Technology 2012. All rights reserved.

Author .....  
Department of Electrical Engineering and Computer Science  
May 18, 2012

Certified by.....  
John G. Kassakian  
Professor of Electrical Engineering and Computer Science  
Thesis Supervisor

Accepted by .....  
Leslie A. Kolodziejski  
Chair, Department Committee on Graduate Theses



# A Generalized Approach to Planar Induction Heating Magnetics

by

Richard Yi Zhang

Submitted to the Department of Electrical Engineering and Computer Science  
on May 18, 2012, in partial fulfillment of the  
requirements for the degree of  
Master of Science

## Abstract

This thesis describes an efficient numerical simulation technique of magnetoquasistatic electromagnetic fields for planar induction heating applications. The technique is based on a volume-element discretization, integral formulation of Maxwell's equations, and uses the multilayer Green's function to avoid volumetric meshing of the heated material. The technique demonstrates two orders of magnitude of computational advantage compared to existing FEM techniques. Single-objective and multi-objective optimization of a domestic induction heating coil are performed using the new technique, using more advanced algorithms than those previously used due to the increase in speed. Both optimization algorithms produced novel, three-dimensional induction coil designs.

Thesis Supervisor: John G. Kassakian

Title: Professor of Electrical Engineering and Computer Science



## Acknowledgments

My work would not have been possible without the mentorship of my advisor, Prof. John G. Kassakian. My deepest gratitude to Prof. Kassakian for his guidance and support, and for providing me the environment to pursue my interests.

Much of the numerical foundations of this work resulted from helpful discussions with Prof. Jacob K. White, who kindly and patiently shared his insights with me.

I am grateful to Yang Wang of The Vollrath Company for her industry perspectives, and for supporting the experimental portions of my work. I would also like to thank Laurent Jeanneteau of Electrolux Major Appliances Europe for our extensive conversations.

My MIT experience has been greatly shaped by the friends I have made over the past two years at Ashdown, in EECS, the GSC and the Energy Club. I would like to thank all of my officemates for our interesting and insightful conversations, as well as our spontaneous technical discussions. I would like to thank my girlfriend Amy for making everything so much fun.

Finally, I am forever indebted to my parents for all the sacrifices they have made for me throughout my life.

The financial support of the William Georgetti Charitable Trust and the John R. Templin Scholarship Trust are gratefully acknowledged.



# Contents

<b>1</b>	<b>Introduction</b>	<b>13</b>
1.1	Motivation . . . . .	13
1.2	Proposed Method . . . . .	16
<b>2</b>	<b>The Induction Heating Process</b>	<b>17</b>
2.1	Equivalent Circuit Model . . . . .	17
2.2	The MQS Electromagnetic Formulation . . . . .	19
2.2.1	Mutual Impedance . . . . .	20
2.2.2	Skin and Proximity Effect Losses . . . . .	22
2.3	Analytical Methods . . . . .	22
2.4	Numerical Methods . . . . .	25
2.4.1	Domain methods . . . . .	25
2.4.2	Integral methods . . . . .	25
2.5	The Partial Element Equivalent Circuit (PEEC) Method and FastHenry	26
<b>3</b>	<b>The PEEC Planar Induction Heating Field Model</b>	<b>29</b>
3.1	The Multilayer Green's Function Approach to Eddy Currents . . . . .	30
3.2	Derivation of the Multilayer Green's functions . . . . .	34
3.2.1	The Dyadic Green's Function for the Semi-Infinite Half-Space	35
3.2.2	The Dyadic Green's function Multiple-Layered Configuration .	39
3.2.3	Application of Numerical Hankel Transforms . . . . .	46
3.3	Evaluation of the Modified Green's Function via Quadrature . . . . .	47
3.4	Eddy Current Loss Profile . . . . .	51

3.4.1	Theoretical Basis . . . . .	52
3.4.2	Implementation Details . . . . .	53
3.5	Comparison to Previous Analytical Models . . . . .	54
3.5.1	Acero et al. . . . .	55
3.5.2	The effect of discretization . . . . .	55
3.6	Experimental Validation . . . . .	57
3.7	Performance . . . . .	64
<b>4</b>	<b>Optimal Design of an Induction Cooktop</b>	<b>67</b>
4.1	The Fitness Function . . . . .	68
4.1.1	Encoding Algorithm . . . . .	68
4.1.2	The Electromagnetic Model . . . . .	69
4.1.3	Scoring Algorithm . . . . .	70
4.2	Single-Objective Optimization of Temperature Profile . . . . .	73
4.3	Multi-Objective Optimization of Temperature, Efficiency and Cost . .	78
<b>5</b>	<b>Conclusions and Future Work</b>	<b>83</b>

# List of Figures

1-1	Illustration of an induction cooktop . . . . .	14
2-1	Lumped parameter transformer model for an induction heating system	17
2-2	Four-element model for an induction heating system. . . . .	18
2-3	Illustration of the Dodd and Deeds two-conductor plane system . . .	23
2-4	The circular filament approximation of the circular spiral . . . . .	24
3-1	Geometries of the point current source above a semi-infinite surface .	36
3-2	Geometry of the point current source within the multilayered configura- tion . . . . .	40
3-3	Comparison between our filament model and measurements by Acero et al. . . . .	56
3-4	The relative errors of our filament model . . . . .	57
3-5	Comparison between the circular filament exact solution and results generated by piecewise linear discretization . . . . .	58
3-6	Relative errors of the piecewise linear approximation of the circular filament . . . . .	59
3-7	Dimensions of the measured litz wire coil . . . . .	61
3-8	Measurements of the coil terminal impedance with and without the load	62
3-9	Comparison of experimentally measured coil impedances with simu- lated results . . . . .	63
4-1	Series resistance for a loop of wire of different constructions . . . . .	71
4-2	Finite difference method stencil of the thermal system . . . . .	73

4-3	Original coil used as the starting point of the optimization analysis . . . . .	75
4-4	Improved coil after 2500 simulated annealing optimization iterations . . . . .	75
4-5	Improved coil at the end of the hybrid pattern search . . . . .	76
4-6	Comparison of the heat and temperature profiles of the designs . . . . .	76
4-7	Heat and Temperature profiles of the three designs in 3D . . . . .	77
4-8	Comparison of single-objective optimized coil designs . . . . .	79
4-9	Results from multi-objective optimization with the NSGA-II Genetic Algorithm . . . . .	81
4-10	Comparison of multi-objective optimized coil designs . . . . .	82

# List of Tables

3.1	Speed benchmark of the axial-symmetric formulation. . . . .	64
3.2	Speed benchmark of the 3D Formulation . . . . .	65
3.3	Comparison of mutual impedance computation speeds with established PEEC tools . . . . .	66



# Chapter 1

## Introduction

In domestic applications, induction heating is most commonly found as the induction cooktop (see Figure 1-1). Unlike traditional flame- or element-based appliances, the induction cooktop heats its vessel directly by the use of a varying magnetic field. This magnetic field is generated within the cooktop by a flat spiral work coil, in turn driven by a high frequency power inverter connected to an ac supply. A tempered glass spacer is used to physically separate the work coil and associated electronics from the corrosive kitchen environment above, and also to protect the work coil from the heat of the cooking vessel. Electromagnetic shielding is usually placed below the work coil (not shown) to reduce the radiated magnetic flux, and to enhance the magnetic coupling between the coil and the vessel [1].

Induction cooktops offer several distinct advantages for the culinary end users when compared to traditional cooking appliances. By avoiding the use of hot heating elements, inflammable gases and open flames, induction cooktops are safer and easier to clean. Thermal inertia is reduced, and this allows their power outputs to be adjusted and controlled with great precision. Moreover, their high energy efficiency lowers energy costs and can considerably abate ambient heating to the rest of the kitchen.

### 1.1 Motivation

The design of the induction coil at the heart of the cooktop is a crucial but complicated process, because it lies at the crossroads of circuit theory, electromagnetism and thermal physics. A great coil design must balance several competing design considerations, including its cost of manufacture, its compatibility with the associated power electronics, its efficiency and the temperature profile of its associated load:

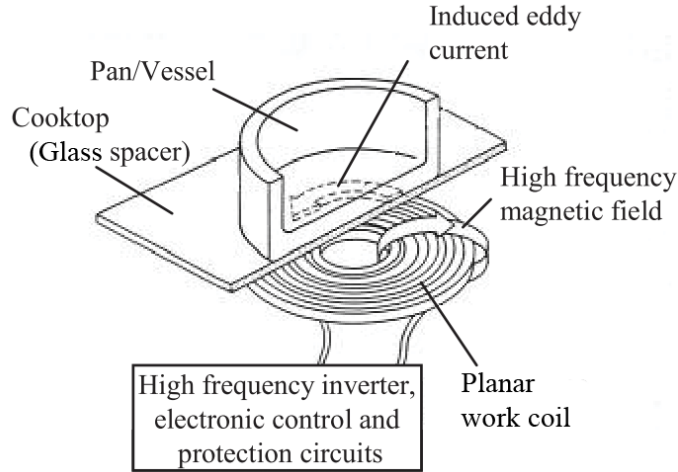


Figure 1-1: Illustration of an induction cooktop [2]

**Material and manufacturing costs.** An induction heating coil is typically made up of several specialized parts. The induction coil itself is usually wound copper litz wire, and the cost of the coil is sensitive to the length and gauge of the wire used. The ferrite shielding that is placed underneath the coil to shield the underside of the heater is also made from an expensive material, and is another significant contributor to costs.

**Electrical Impedance ( $Z_{eq}$ ).** The impedance of the coil is the ratio and phase difference between the terminal voltage and current of the work coil. The impedance is intimately tied to the costs of the power electronic converter used to drive the coil. As the coil impedances increases, components with lower current ratings can be used in the converter, bringing both cost savings and increases in efficiency to the overall system.

**Transfer Efficiency ( $\eta_{ind}$ ).** The transfer efficiency is defined as the ratio between the power transferred to the load  $P_D$  and the total power supplied  $P_T$ . The power not transferred to the load is dissipated as loss within the coil itself. Let  $P_C$  be the power dissipated in the work coil; the transfer efficiency can be expressed as:

$$\eta_{ind} = \frac{P_D}{P_T} = \frac{P_D}{P_D + P_C} \quad (1.1)$$

Inefficiencies in the transfer of power is undesirable because it causes the induction coil to heat up, reducing its lifetime and increasing its failure rate. Excessive losses also drives the cost and weight of the cooling system, which must be sized to dissipate the undesirable heat. Moreover, a range of efficiency standards are imposed on electric

appliances in some parts of the world, and the transfer efficiency of the induction cooktop must be specially designed for these markets.

**Heating and Temperature Profile.** The heating profile describes the distribution of power output over the bottom of the heated pan, and the temperature profile describes the distribution of steady-state temperature over the pan. These are the criteria that determine the quality of the cooking experience, and therefore are important proxies for consumer satisfaction.

Achieving a balance between all of these considerations is an exercise in multi-objective optimization. With the development of advanced computing technologies, computational design techniques have been applied to a wide range of multi-objective engineering optimizations problems. Regardless of the details, the core idea is to replace the laborious and time intensive task of design by educated guesses and careful experimentation with a systematic process automated by a computer. In particular, two vital tasks are performed on the computer, at speeds many orders of magnitude faster than those previously obtainable:

1. The intermediate experimental verification step, where successive iterations of design are analyzed and assessed, is replaced by a software numerical optimization model.
2. Educated trial-and-error is replaced by numerical optimization algorithms that systematically explore the design space for better designs.

Compared to conventional design by experimental verification, computational techniques can analyze and assess many more designs in a span of time, without incurring extensive costs in prototyping. For these reasons, the computational design approach is found in a wide range of engineering applications, from the design of structures to communications and electronic devices [3, 4].

However, the computational design approach has mostly eluded domestic induction heaters [5], due to the absence of the most vital ingredient – a fast and accurate computational technique. While fast analytical models of planar induction heating physics have existed since 1968 [6, 7, 8, 9, 10, 11, 12], a large collection of assumptions are necessary for these analytical solutions to exist, such as rotational symmetry, linearity, isotropy, homogeneity. These assumptions limit the predictive power of the models and the degree of freedom available to the designer. For these reasons, the usefulness of the analytical models is restricted to a limited set of conventional designs.

In more recent years, the finite element method (FEM) has become a favored analysis tool for the design of domestic induction heating coils [13, 14]. In comparison

to the analytical methods above, FEM is numerically stable without being tied to any underlying assumptions. Today, many commercial software exist that can evaluate the physics of induction heating to an arbitrary level of precision [15]. Unfortunately, FEM is also a very computationally expensive approach, because it relies on the meshing of a volume of space into fine elements. Each individual FEM evaluation can take from a few minutes to a few hours to complete. For this reason, the value of FEM is mostly in design verification, rather than in the design process itself.

## 1.2 Proposed Method

The following thesis applies the computational approach to the design of an induction cooktop. The novelty is in the computational method used, based on a volume-element discretization, integral formulation of the magnetoquasistatic Maxwell's equations known as the Partial Element Equivalent Circuit (PEEC) method [16]. The method is used to evaluate the electromagnetic fields of three-dimensional coils placed above or sandwiched between layered conductive magnetic materials. Unlike existing analytical, FEM and integral-formulation methods, our PEEC method is optimized for speed and accuracy by exploiting the rotational and translational symmetries inherent in the planar induction heating problem. The dyadic multilayer Green's function is used to capture the effects of eddy currents, without explicitly modeling the eddy currents flowing in the conductor. By avoiding volume-discretization in the heated load, the evaluation speed is greatly increased.

The foundational knowledge required to understand the work contained within this thesis is presented in Chapter 2. In Chapter 3, the numerical formulation of this PEEC model is presented, and the implementation techniques are discussed. Results on the accuracy and speed of the method are shown.

In Chapter 4, the PEEC model is used to perform the computational design and optimization of an induction cooktop. The high speed and generality of the model allows advanced optimization algorithms to be used to explore many degrees of freedom in the design of the coil. In particular, simulated annealing—a mathematically sufficient algorithm for finding the global optimum [17]—is used to generate a spiral coil optimized for the uniformity of the load temperature profile. Furthermore, multi-objective genetic algorithms are used to study the multi-objective optimization problem.

# Chapter 2

## The Induction Heating Process

Induction heating traces its origins to the very early days of electromagnetism. Heating by eddy currents was first discovered in 1865 by Leon Foucault, while experimenting with a rotating copper disc placed inside a permanent magnetic field. The first practical attempts at induction heating dates back to 1891, and the theoretical basis was established by the luminaries of electrical engineering, including Hertz, Heaviside, Thomson, Ewing and others [18].

### 2.1 Equivalent Circuit Model

While its physics are strictly governed by Maxwell's equations, the electrical properties of induction heating are more easily understood in the context of an equivalent circuit model. One common approach is to model the magnetic interaction between the excited induction coil and the load as that of a standard transformer [8]. The equivalent circuit for such a model is shown in Figure 2-1.

The lumped circuit elements included here are the primary coil resistance  $R_C$ ,

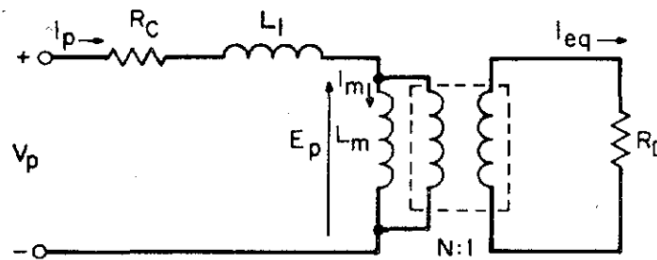


Figure 2-1: Lumped parameter transformer model for an induction heating system [8]

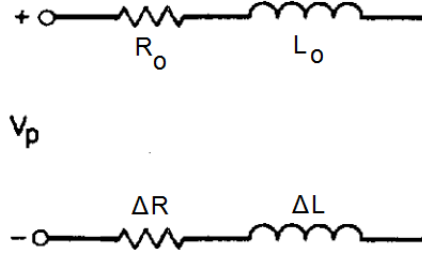


Figure 2-2: Four-element model for an induction heating system.

leakage inductance  $L_l$ , magnetizing inductance  $L_m$ , turns ratio  $N$  and the load resistance  $R_D$ . When a voltage  $V_p$  is applied to the terminals of the induction coil, primary current  $I_p$  flows into the coil, inducing a voltage across  $L_l$  and  $L_m$ , but also causing some losses to occur due to the presence of  $R_C$ . The voltage induced across  $L_m$  is transformed  $N:1$  steps down, where it appears as a voltage across the load resistance  $R_D$ . With some minor algebra, the transfer efficiency  $\eta_{ind}$  can be expressed in terms of the lumped parameter component values:

$$\eta_{ind} = \frac{R_R}{R_R + R_C (1 + R_R^2/X_m^2)} \quad (2.1)$$

Here,  $R_R = N^2 R_D$  is the resistance of the load reflected to the primary. It can be seen that the transfer efficiency is solely determined by the load resistance, winding resistance, and the magnetizing impedance.

A simpler but less physically intuitive approach used by domestic induction heating researchers is to model the induction heating system as the series connection of two resistors and two inductors [1, 19, 20] (shown in Figure 2-2). Here, the values  $R_0$  and  $L_0$  are the resistance and inductance of the primary coil in free-space, and the values  $\Delta R$  and  $\Delta L$  are the changes in terminal resistance and inductance due to the presence of the load. It is readily shown that this model is related to the previous model by the following equations:

$$R_0 = R_C \quad (2.2)$$

$$\Delta R = \frac{N^2 R_D}{1 + (R_R/\omega L_m)^2} \quad (2.3)$$

$$L_0 + \Delta L = L_l + \frac{L_m}{1 + (\omega L_m/R_R)^2} \quad (2.4)$$

With the four-element model, the transfer efficiency is reduced to a simple relation

between the two resistances:

$$\eta_{ind} = \frac{\Delta R}{R_0 + \Delta R} \quad (2.5)$$

It is clear from this relation that improvements in efficiency will come from an increase in  $\Delta R$  or a reduction in  $R_0$ .

Delving deeper into the circuit elements will require an understanding of the electromagnetic field interactions that allow induction heating to occur. In particular, the parameters  $L_0$ ,  $\Delta L$  and  $\Delta R$  are the resultant of the magnetic coupling that exist between the coil and the load. The foundational formulation of Maxwell's Equations are derived in Section 2.2, and a brief introduction to the modeling of magnetic coupling via mutual impedances is given in Section 2.2.1. The value of  $R_0$  also becomes strongly affected by electromagnetic fields at higher frequencies, due to the skin and proximity effect; these effects are discussed in Section 2.2.2.

## 2.2 The MQS Electromagnetic Formulation

Maxwell's equations solely govern the physics of practical induction heating, but the magnetoquasistatic (MQS) approximation is often used to reduce their complexity. In the conditions where frequencies rarely exceed a few hundred kilohertz, the MQS form of Maxwell's equations is able to predict electromagnetic fields to high precision [21].

Maxwell's equations have the following form for linear, homogenous and isotropic media under MQS conditions:

$$\nabla \times \mathbf{B} = \mu \mathbf{J} \quad (2.6)$$

$$\nabla \times \mathbf{E} = -\frac{\delta}{\delta t} \mathbf{B} \quad (2.7)$$

The simplification made by the MQS assumption is to set both displacement current  $\delta \mathbf{D} / \delta t$  and volumetric free charge  $\rho_f$  to zero. The physical interpretation of this is that all parasitic capacitances are neglected. The assumption allows the magnetic potential vector  $\mathbf{A}$  to be defined with the Coulomb gauge as:

$$\nabla \times \mathbf{A} = \mathbf{B} \quad (2.8)$$

$$\nabla \cdot \mathbf{A} = 0 \quad (2.9)$$

Combining (2.6)-(2.9) yields the well-known diffusion Helmholtz equation for time-

harmonic MQS systems:

$$\nabla^2 \mathbf{A} = j\omega\mu\sigma\mathbf{A} - \mu\mathbf{J}_{src} \quad (2.10)$$

The right hand side of the equation describes the currents that flow within the system, and the left hand side describes the magnetic fields that are generated by these currents. The first term on the right accounts for the induced eddy currents; the presence of  $\mathbf{A}$  in this term highlights its causal relationship with the system magnetic fields. Clearly eddy currents will not flow if a material is non-conductive ( $\sigma = 0$ ) or completely diamagnetic ( $\mu = 0$ ), and under these conditions this particular term is reduced to zero. The second term on the right accounts for the source currents that are impressed upon the system, i.e. the currents in the coil.

For a system excited with a current  $J_{src}$ , equation (2.10) can be solved with a wide range of numerical and analytical tools to give  $\mathbf{A}$  fields at all points in the system. The magnetic field  $\mathbf{H}$  and the magnetic flux density  $\mathbf{B}$  can be solved by applying the definition equation of the magnetic vector potential (2.8), and the electric field  $\mathbf{E}$  can be obtained by applying Faraday's law (2.7):

$$\mathbf{E} = -j\omega\mathbf{A} \quad (2.11)$$

$$\mathbf{H} = \frac{1}{\mu}\nabla \times \mathbf{A} \quad (2.12)$$

Thus, for a given geometry of filaments and materials, the electromagnetic fields of the system are fully characterized once the  $\mathbf{A}$  fields are characterized. Numerical techniques for calculating the  $\mathbf{A}$  fields are discussed further in Section 2.4.

## 2.2.1 Mutual Impedance

In circuit theory, the mutual impedance concept quantifies the coupling between the otherwise isolated elements in a circuit. In MQS systems where capacitances are zero, mutual impedance exists between different current-conducting elements due to the magnetic coupling between them. When current flows through a conductor, a magnetic field is created according to Ampere's law (2.6), and this magnetic field in turn induces an electric field according to Faraday's law (2.7). If a second conductor is placed within this electric field, then a voltage is induced across this conductor according to:

$$V = \int_{contour} \mathbf{E} \cdot d\mathbf{s} \quad (2.13)$$

Here, the line integration takes place along the contour of the second conductor. The *mutual impedance*  $Z_m$  (with units of Ohms or  $\Omega$ ) is defined to be the ratio between the voltage induced across the second conductor and the current that flows through the first conductor, i.e. for conductors 1 and 2:

$$Z_m = \frac{1}{I_1} \int_{cond2} \mathbf{E}_1 \cdot d\mathbf{s} \quad (2.14)$$

$I_1$  is the current through conductor 1,  $\mathbf{E}_1$  is the electric field induced by conductor 1, and the integration is performed along the contour of conductor 2. Due to the reciprocity of electromagnetism, the mutual impedance of the two conductors is always equal, regardless of the order of excitation and integration. It is interesting to note that each of the conductors also exhibits mutual impedance with itself. This effect is named the *self-impedance*, but is more commonly known simply as the *impedance* of the conductor.

The self- and mutual-impedance concepts are used in induction heating to calculate the terminal impedance of the induction coil. In the four-element model of Figure 2-2, the total terminal impedance of the coil is equivalent to the self-impedance of coil, in the presence of the load. To calculate this value, the coil is excited with a known current to produce a magnetic field that induces eddy currents in the load according to the diffusion Helmholtz equation (2.10). This changing magnetic field induces an electric field according to Faraday's law (2.7). The voltage induced across the coil can then be measured by a line integral along the contour of the coil according to (2.13). Here, the integrand contains contributions to the electric field generated by both the coil as well as the induced eddy currents in the load.

However in most realistic cases, the line integral along the contour of the coil can be difficult to solve, and the geometry of the coil may not have an associated closed-form expression. In these cases, the calculation can be simplified by subdividing the coil into a collection of linear filaments. The self- and mutual- impedance of and between each of these filaments can be separately evaluated, by exciting one piece of the coil at a time and performing the integration independently for each filament. Since the filaments are connected in series, these self- and mutual- impedances of each component filament can be summed together to result in the self-impedance of the combined coil.

It is important to note that each linear piecewise filament by itself does not form a complete loop, and the resultant field that it produces does not satisfy all of Maxwell's equations. Therefore, the impedances associated with the piecewise filaments can-

not be considered in the same sense as closed-loop impedances. In literature, these impedances are often referred to as partial impedances, to distinguish them from loop impedances.

The calculation process for the transformer model shown earlier in Figure 2-1 is related but not identical to the procedure described above. An extensive discussion on how the magnetizing inductance  $L_m$ , leakage inductance  $L_l$ , and the load impedance  $R_D$  of Figure 2-1 are related to the mutual impedances of the filaments can be found in [8].

### 2.2.2 Skin and Proximity Effect Losses

The skin and proximity effects are names for the tendency of high frequency electric currents to distribute themselves at the outer surfaces of conductors. Because of these effects, the effective resistance of the conductors tend to increase dramatically at high frequencies and also become frequency dependent. The effects stem from opposing eddy currents induced by magnetic fields, in turn a resultant of the currents that flow within the wires. When the magnetic field is self-induced by the same conductor experiencing the eddy currents, the increase in effective resistance is known as the *skin effect*. When the source of the magnetic field are external elements in proximity to the conductor, the effect is known as the *proximity effect*.

The skin and proximity effects can adversely affect the transfer efficiency of the induction system according to (2.5). For the loss of efficiency to be controlled and contained, one common technique is to use wires with strands that are individually insulated from each other. The term *litz wire* is used to describe a special kind of stranded wire, carefully woven in a pattern that minimizes the skin and proximity effects. Due to their high frequency and high efficiency requirements, the vast majority of domestic induction coils are wound with stranded or litz wire [1]. Thorough mathematical models have been developed in literature to study the frequency-dependent resistances of plain and litz wires [20, 22, 23].

## 2.3 Analytical Methods

Many of the first investigators of induced eddy currents came from the related fields of non-destructive eddy current testing and from microelectronics, and analytical solutions had been derived for convenient symmetries. The first analytical solution of the planar eddy current problem is often credited to Dodd and Deeds [6]. In

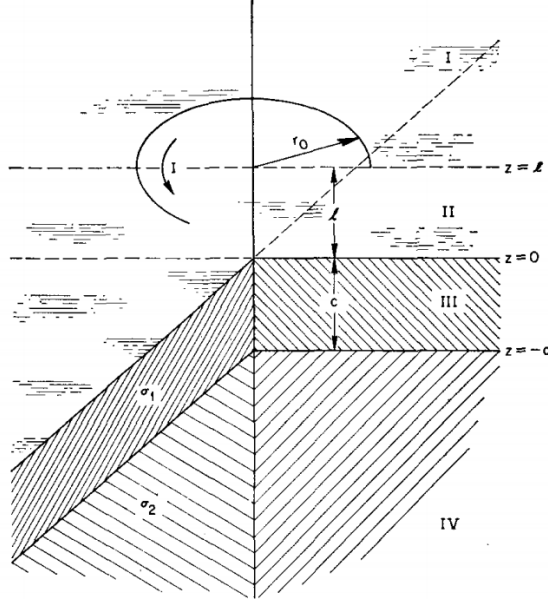


Figure 2-3: Illustration of the Dodd and Deeds two-conductor plane system [6]

their seminal 1968 paper, they discussed the system where a single circular coil of infinitesimal thickness is suspended above a two-conductor infinite plane, as shown in Figure 2-3. By using the general solution to the Bessel equation to solve the diffusion Helmholtz equation in cylindrical coordinates, they were able to express the magnetic potential vector as an analytical solution in the form of the Sommerfeld integral:

$$A_{\phi}^{(j)}(r, z) = \frac{\mu_j I_{\phi} r_0}{2} \int_0^{\infty} G_j(k, z) J_1(kr_0) J_1(kr) dk \quad (2.15)$$

where for the  $j$ -th region,  $\mu_j$  is its magnetic permeability and  $G_j(k, z)$  is some expression that characterizes the behavior of that region.  $J_1$  is the first order Bessel function of the first kind. Defining the first-order Hankel transform to be

$$f(r) = \mathcal{H}_1^{-1} [F(k)] = \int_0^{\infty} F(k) J_1(kr) k dk \quad (2.16)$$

and following that:

$$\mathcal{H}_1^{-1} [I_{\phi} r_0 J_1(kr_0)] = I_{\phi} \delta(r - r_0)$$

(2.15) can be recognized as the convolution integral between the Green's function and a ring of current with radius of  $r_0$ , under the first-order Hankel transform:

$$A_{\phi}^{(j)}(r, z) = \frac{\mu_j I_{\phi}}{2} \mathcal{H}_1^{-1} [G_j(k, z)] * \delta(r - r_0)$$

It is important to note that the Dodds and Deeds result is a rotationally symmetric solution for the circular closed loop. While not strictly rotationally symmetric, flat spirals can be modeled to good accuracy as the series connection of concentric circular turns [11, 24, 25] (see Figure 2-4). With this approximation, the fields generated by each turn is superimposed together to obtain the total field of the entire spiral. In more recent years, the Dodds and Deeds solution has been extended to microelectronic inductors [24, 25] and induction cooktops [19, 11].

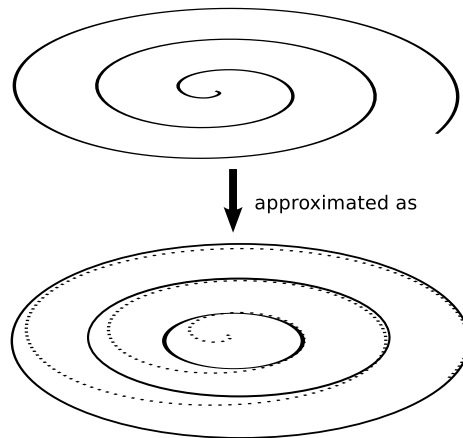


Figure 2-4: The circular filament approximation of the circular spiral

While fast and elegant, these analytic solutions do pose several concerns. Firstly, due to the use of the Green's function, superposition is implied at the formulation stage. For these solutions to be valid, all materials must be linear, isotropic and homogenous. These constraints preclude hysteresis from being modeled. Secondly, the analytical formulations impose rotational symmetry upon the shape of the coil. Noting the fact that the bulk of cookware are also circular, this is not a significant issue for the design of a basic induction cooktop. However, it does pose a problem when more creative designs are considered. For example, a three-layer array of hexagonal coils has been proposed in the related field of induction power transfer. This novel arrangement has been shown to generate a perfectly uniform magnetic field [26]. As they currently stand, none of these existing analytical formulations can be directly applied because the system analyzed cannot be approximated as rotationally symmetric.

## 2.4 Numerical Methods

Numerical methods have been developed as the response to practical engineering problems with complicated boundary conditions and irregular geometries, where analytical solutions often do not exist. Combined with advances in computing hardware, numerical methods have become an indispensable tool in the analysis of induction heating systems.

### 2.4.1 Domain methods

The most well-known numerical methods are domain methods, such as the finite difference method (FDM) and the finite element method (FEM). Here, the domain of the problem is discretized into some subdomains, and the problem is evaluated at special points such as the intersection of subdomains or Gaussian quadrature points. Maxwell's equations are reduced into a finite set of linear algebraic equations at these evaluation points, and the equations are solved as a matrix inversion problem using LU decomposition or an iterative technique such as GMRES or the Biconjugate Gradient method. [27]

The domain methods differ in how these subdomains are formulated and how the linear equations are derived. In the FDM, the subdomains are constructed using a grid formation, and the derivative operator is approximated with differences between adjacent subdomains. In the FEM, the subdomains are constructed with elements, each defined by a set of basis functions. The governing differential equations are solved by a set of trial functions, and integration is performed analytically or by Gaussian quadrature.

### 2.4.2 Integral methods

Integral methods, such as the boundary element method (BEM), boundary integral method (BIM) and the method of moments (MoM), constitute an alternative set of numerical methods. These methods reformulate Maxwell's equations as a set of boundary integral equations by a combination of mathematical techniques such as the weighted residual method, integration by parts, Green's identities, Green's theorem, the Divergence theorem and Stoke's theorem. The boundary integral equation is then discretized and transformed into a set of linear equations by analytical integration or by Gaussian quadrature, and the equations are again solved as a matrix inversion problem.

Unlike domain methods, integral methods require only the discretization of the boundary of the domain, one dimension less than the domain itself. As a result, mesh generation is greatly simplified, and the total degrees of freedom is significantly reduced. The application of the Green’s function also allows boundary conditions to be implicitly specified at infinity. [27]

One major downside to the integral methods is the fact that they usually result with densely packed linear equations, that can be evaluated and solved only with  $\mathcal{O}[N^2]$  speed even with iterative methods. Fortunately in many cases, compression techniques such as multipole expansion and adaptive grids can increase solve speeds to  $\mathcal{O}[N]$  or  $\mathcal{O}[N \log N]$ . These techniques are not general, and must be applied on a case by case basis.

## 2.5 The Partial Element Equivalent Circuit (PEEC) Method and FastHenry

The Partial Element Equivalent Circuit Method (PEEC) first described by Ruehli [16] is a volume-element discretization, integral formulation technique for the analysis of complex 3D circuit elements. According to the PEEC method, complicated conductor geometries are discretized as volume elements of straight filaments, interconnected in series and parallel. Each of these filaments is electromagnetically coupled with other filaments according to self- and mutual- impedance terms. Once these impedance terms are found, the filaments are connected together into an equivalent circuit. The equivalent circuit is then quickly solved as a SPICE simulation.

The mathematical formulation of the PEEC as an electric field equation is the following:

$$\frac{\mathbf{J}(\mathbf{r})}{\sigma} + \frac{j\omega\mu}{4\pi} \int_{V'} \frac{\mathbf{J}(\mathbf{r}')}{\|\mathbf{r} - \mathbf{r}'\|} dv' = -\nabla\Phi(\mathbf{r}) \quad (2.17)$$

where  $\mathbf{J}$  is the current density and  $\Phi$  is the scalar potential. The first term on the left is the resistive contribution at the field point  $\mathbf{r}$ , and the second term is the inductive contribution by all source points  $\mathbf{r}'$  within the domain of interest  $V'$ .

The PEEC is most famously implemented in FastHenry [28], a magnetoquasistatic (MQS) inductance extraction tool for complex 3D circuits in free-space-like conditions ( $\mu = \mu_0, \epsilon = \epsilon_0, \sigma = 0$ ), ubiquitously used in the field of microelectronics and integrated circuits. As an MQS tool, FastHenry ignores all capacitances inherent

between filaments, so that only the partial self- and mutual- inductances of the filaments are evaluated. Current flow within a long thin conductor is assumed to flow parallel to its surface, so that there is no charge accumulation on the surface. When a geometry is inputted, FastHenry breaks all conductors down into smaller filaments along their lengths, widths and heights. Each filament is designated as a branch of a large mesh, and the Z matrix is formed that will relate each branch voltage to each branch current:

$$V_b = ZI_b = (R + j\omega L)I_b \quad (2.18)$$

Once the Z matrix is created, the equivalent circuit system is solved via mesh analysis. Here, Kirchoff's voltage law for the conservation of voltage can be written as:

$$MV_b = V_s \quad (2.19)$$

where  $V_s$  is the mostly zero vector of source branch voltages, and the matrix  $M$  defines the set of meshes within the system. The same mesh matrix must also satisfy:

$$M^T I_m = I_b \quad (2.20)$$

where  $I_m$  is the vector of mesh currents. Combining (2.18), (2.19) and (2.20) yields:

$$MZM^T I_m = V_s \quad (2.21)$$

This equation is then inverted with an iterative algorithm to result in a mesh current solution.

One of the most computationally expensive parts of FastHenry is the formation of the dense Z matrix, where self- and mutual- partial inductances are evaluated. Solving the partial inductance for two filaments  $k$  and  $m$  requires the evaluation of the integral: [16]

$$L_{p.km} = \frac{\mu_0}{4\pi} \frac{1}{a_k a_m} \int_{a_k} \int_{a_m} \int_{b_k}^{c_k} \int_{b_m}^{c_m} \frac{|\mathbf{dl}_k \cdot \mathbf{dl}_m|}{r_{km}} da_k da_m \quad (2.22)$$

for every filament pair within the system. The terms  $a_k$  and  $a_m$  are the cross-sectional areas of the two filaments, the limits of integration  $b_k$ ,  $b_m$  and  $c_k$ ,  $c_m$  represent the start and end points of the two filaments respectively, and  $r_{km}$  is the Euclidean distance between the points of integration. The challenge that the Z matrix presents is that its number of elements grows according to  $\mathcal{O}[N^2]$ , and that the terms cannot be arbitrarily truncated for it to remain numerically stable [29]. In FastHenry's

implementation, these challenges are overcome in two ways:

- For close-by interactions, FastHenry is programmed with a plethora of closed-form analytical solutions to (2.22) from [30], [31], [32] and [16]. These solutions avoid the need for numerical integration to be used.
- For far-away interactions, FastHenry uses the Fast Multipole Method (FMM) to compress many far-away filaments and to solve them together directly as point sources. The FMM reduces the order of the problem to  $\mathcal{O}[N]$ .

These efficient techniques for obtaining the L matrix, along with clever preconditioning of the iterative solver, are the secrets to FastHenry's speed. Note that both of these techniques inherently require the Green's function for magnetic interactions to be that of the free-space solution to Laplace's equation. This hard requirement on the form of the Green's function limits FastHenry's usefulness in applications where conductive, magnetic materials are used.

## Chapter 3

# The PEEC Planar Induction Heating Field Model

The accurate prediction of electromagnetic fields is crucial for the eddy current analysis of induction heating. Over the past thirty years, a wealth of literature has been built around modeling the electromagnetic fields of eddy current processes using numerical simulation techniques. Today, there are several commercial software packages that can accurately treat complex eddy current physics coupled with non-linear material properties, thermal processes and mechanical deformations [15]. However, for the purposes of computational design and optimization, the speed of the field solver is also important. In literature, order reduction and computational acceleration is typically achieved either through enforcing rotational symmetry [14, 33], or through enforcing the so called “Manhattan symmetry”, where all heights, widths and lengths are either parallel or perpendicular to each other [34, 35, 36].

In this chapter, we present a fast, fully three-dimensional electromagnetic field solver based on the Partial Element Equivalent Circuit method (PEEC) that analyzes non-symmetrical conductor structures placed on top, or sandwiched within infinite-extent, multilayered media. This model encapsulates a large collection of problems including induction cooking [1], planar monolithic inductors and transformers [24, 34, 37], microelectronic power and ground planes [35] and non-destructive eddy testing systems [38].

The computational advantage gained by our method comes from its minimization of volumetric meshing. As an integral formulation of Maxwell’s equations, PEEC requires only the meshing of conductive domains where current flow is expected [16], rather than over the entire system domain as in the case for domain formulation techniques such as the finite element method (FEM) and the finite difference method

(FDM). However in traditional PEEC method solvers like FastHenry [28], much of this advantage is eroded away in the presence of a large conductive domain, such as a ground plane or conductive substrate in the case of microelectronics, or a heated load in the case of induction heating. The traditional PEEC formulation requires the entire conductive volume to be meshed in order to account for the internally varying current flows [28]. This process dramatically increases the size of the problem and reduces the computational speed of the PEEC method.

Other integral formulations such as the boundary element method (BEM), boundary integral method (BIM) and the boundary integral equation method (BEIM) have been successfully used to replace the volumetric mesh over the conductive domain with a surface mesh over its boundary [39, 40, 41, 42]. This is particularly efficient when the skin depth is negligible relative to the dimensions of the conductive domain, and the induced current is zero throughout most of the volume [27]. However on a per element basis, the formation of boundary mesh elements is more computationally expensive, because each element tends to be tightly coupled with all other elements in the system.

In the method presented in this chapter, the PEEC method is modified to avoid the explicit treatment of the conductive domains. With the assumption that the conductive domain can be approximated as an infinite-extent and uniform thickness plane, the multilayer Green’s function can be derived to implicitly capture the effects of the eddy currents induced within it. The multilayered Green’s function is then embedded into the PEEC framework, and the volumetric meshing of the conductive domain is avoided altogether. In previous multilayer Green’s function / PEEC approaches [37, 35], the convolution integral is resolved using the two-dimensional FFT, restricting the conductors to cartesian Manhattan symmetry. In the following work, singularity-subtraction quadrature rules are used to expand the method to all three-dimensional conductor arrangements.

### 3.1 The Multilayer Green’s Function Approach to Eddy Currents

Magnetoquasistatic (MQS) systems with eddy currents are governed by the diffusion Helmholtz equation:

$$(\nabla^2 - j\omega\mu\sigma)\mathbf{A} = -\mu\mathbf{J}_{\text{src}} \tag{3.1}$$

Here,  $\mathbf{A}$  is the magnetic potential vector and  $\mathbf{J}_{\text{src}}$  is the current density of the excitation currents. If linearity and isotropism are assumed, (3.1) can be rewritten as a convolution integral equation:

$$\mathbf{A}(\mathbf{r}) = \int_{V'} \overline{\overline{\mathbf{G}}}(\mathbf{r}, \mathbf{r}') \cdot \mathbf{J}(\mathbf{r}') dv' \quad (3.2)$$

where  $\mathbf{r} = (x, y, z)$  is the point of field evaluation,  $\mathbf{r}' = (x', y', z')$  is one point source of magnetic fields, and the region of integration  $V'$  is the excitation currents within the system. Each component of the kernel of integration  $\mathbf{G}_{\{x,y,z\}}(\mathbf{r}, \mathbf{r}')$  is the solution to the magnetic diffusion Helmholtz equation for a point current source  $\hat{x}$ ,  $\hat{y}$ , or  $\hat{z}$  direction:

$$(\nabla^2 - j\omega\mu\sigma)\mathbf{G}_{\{x,y,z\}}(\mathbf{r}, \mathbf{r}') = -\delta(x - x')\delta(y - y')\delta(z - z')\{\hat{x}, \hat{y}, \hat{z}\} \quad (3.3)$$

If (3.3) is solved respecting all boundary conditions between different domains in the  $\hat{z}$  direction, the resultant solution—commonly known as the multilayer Green’s function—would implicitly capture the contributions of the induced eddy currents to the magnetic fields within the system.

The multilayered Green’s function can be embedded into the PEEC formulation [16] as an electric field integral equation:

$$\frac{\mathbf{J}(\mathbf{r})}{\sigma} + j\omega \int_{V'} \overline{\overline{\mathbf{G}}}(\mathbf{r}, \mathbf{r}') \cdot \mathbf{J}(\mathbf{r}') dv' = -\nabla\Phi(\mathbf{r}) \quad (3.4)$$

where  $V'$  excludes the conductive layers above and below the excitation conductors. Using (3.4) with the MQS current conservation law:

$$\nabla \cdot \mathbf{J} = 0 \quad (3.5)$$

the excitation current density  $\mathbf{J}$  and scalar potential  $\Phi$  can be computed. With the excitation current density  $\mathbf{J}$  known, all fields within the system can be reconstructed using the superposition integral (3.2).

Unfortunately, it can often be difficult to efficiently evaluate the integral in (3.4). The integration must be performed over at least three dimensions—a particularly difficult task for most numerical integration techniques. Moreover, the Green’s function contains a singularity at  $\mathbf{r} = \mathbf{r}'$ , and this singularity causes the function to be numerically ill-conditioned when  $\mathbf{r} - \mathbf{r}'$  is small.

In this chapter, both of these issues are tackled through the use of the *singularity*

*subtraction technique.* As discussed above,  $\overline{\overline{G}}(\mathbf{r}, \mathbf{r}')$  is the solution to the diffusion Helmholtz equation (3.1) for the magnetic potential vector  $\mathbf{A}$  at the field point  $\mathbf{r}$  for a point current source at  $\mathbf{r}'$ . Due to the superposition of fields,  $\overline{\overline{G}}(\mathbf{r}, \mathbf{r}')$  contains both a free-space contribution from the current source itself at  $\mathbf{r}'$ , as well as the response of the eddy currents and magnetic domains spread throughout the entire system. For this reason, we can write:

$$\begin{aligned}\overline{\overline{G}}(\mathbf{r}, \mathbf{r}') &= \overline{\overline{G}}_{free}(\mathbf{r}, \mathbf{r}') + \overline{\overline{G}}_{sys}(\mathbf{r}, \mathbf{r}') \\ &= \frac{\mu_0(\hat{x}\hat{x} + \hat{y}\hat{y} + \hat{z}\hat{z})}{4\pi\|\mathbf{r} - \mathbf{r}'\|} + \overline{\overline{G}}_{sys}(\mathbf{r}, \mathbf{r}')\end{aligned}\quad (3.6)$$

It is clear from (3.6) that the singularity within  $\overline{\overline{G}}$  originates through  $\overline{\overline{G}}_{free}$ . Once the singularity is removed, the remainder  $\overline{\overline{G}}_{sys}$  is smoother and easier to integrate. Within this thesis,  $\overline{\overline{G}}_{sys}$  is denoted as the *modified Green's function*.

Rewriting (3.4) with the modified Green's function explicitly isolated:

$$\frac{\mathbf{J}(\mathbf{r})}{\sigma} + \frac{j\omega\mu}{4\pi} \int_{V'} \frac{\mathbf{J}(\mathbf{r}')}{\|\mathbf{r} - \mathbf{r}'\|} dv' + j\omega \int_{V'} \overline{\overline{G}}_{sys}(\mathbf{r}, \mathbf{r}') \cdot \mathbf{J}(\mathbf{r}') dv' = -\nabla\Phi(\mathbf{r}) \quad (3.7)$$

The first two terms of the left hand side and the right hand side correspond exactly with the traditional PEEC formulation as described by Ruehli [16], and they can be efficiently and accurately computed with existing closed-form expressions [30, 31, 32] as implemented in solvers like FastHenry [28]. The modified Green's function term corresponds to the eddy and magnetic domain responses of the system, and must be numerically integrated using quadrature rules. This is a considerably easier task than before with the singularity removed.

The full method within this chapter can be described as a series of steps within the PEEC framework. One significant difference is the introduction of an initial *characterization* stage, where the modified Green's function is computed and tabulated. This step only needs to be performed once for each layered design:

1. **Derivation of the modified Green's function.** The analytical solutions for the dyadic multilayered Green's function are derived by hand for a specified number of layers above and below the coil. The free-space Green's function is isolated and removed during the derivation stage, leaving an analytical expression for the modified Green's function. The mathematics of this step is described in detail in Section 3.2. Here, all of the Green's function are expressed as Hankel transform integrals, and Section 3.2.3 discusses how they can

be quickly evaluated with numerical Hankel transform techniques.

2. **Tabulation.** The modified Green’s function is evaluated and tabulated so that fast look-up table techniques can be used. Due to the inherent rotational symmetry, the system Green’s function is only dependent upon a fixed collection of variables, serving as the axes of this table. These variables are the radial distance of the source and field points  $r - r' = \sqrt{(x - x')^2 + (y - y')^2}$ , the sums and differences of their heights  $(z + z')$ ,  $(z - z')$  and the frequency  $f$ .

Once the layers are characterized, each subsequent induction coil design can be evaluated with the following steps :

1. **Input.** A list of  $N$  filaments is inputted and numbered from 1 to  $N$ .
2. **Formulation of the free-space Z matrix.** For each filament pair, the mutual impedance between them in free-space conditions is calculated using closed-form solutions and stored as a cell within an  $N \times N$  matrix denoted as the Z matrix.
3. **Calculation of the system contribution.** For each cell in the Z matrix, the mutual impedance contribution of the system is calculated by convolving the modified Green’s function via multidimensional sparse grid quadrature. The quadrature equations are (3.68)-(3.70), and (3.73)-(3.75); details on their implementation can be found in Section 3.3. This is the most computationally expensive step of the algorithm.
4. **Solve for system currents.** A known voltage excitation is applied to the terminals of the induction coil. The Z matrix, corrected with the system contribution, is used with the FastHenry implementation of the PEEC method. Mesh analysis is performed, and the linear equations are solved with GMRES to result in a current value for each filament. For details on how the Z matrix is used to solve for system currents, see the original FastHenry implementation [28]. The impedance of the coil is taken to be the ratio between the applied voltage and the terminal current solved through this step.
5. **Solve for fields.** With all the currents known, the fields are solved at areas of interest. Firstly, the free-space contribution is solved at each field point using closed-form solutions. Then, quadrature rules are used to solve for the system contributions, by numerically convolving the modified Green’s function with the known current densities. The fields are used to calculate the induction heat profile according to Section 3.4.

Note that step 4 can be avoided if the conductors are only discretized along their lengths, and not over their cross-sectional areas. As all the filaments are connected in series, the current flowing through all the filaments must be identical. The partial impedances (i.e. each entry of the  $Z$  matrix) can be fused together into a single equivalent circuit element by simple summation, and this value is indeed the terminal impedance of the coil.

## 3.2 Derivation of the Multilayer Green's functions

The multilayer Green's functions for two geometries are presented in this section. The first is the semi-infinite half-space, which has been extensively studied both theoretically and experimentally from the early days of eddy current analysis. The semi-infinite geometry is known to be an accurate model of eddy currents when the penetration depth of the electromagnetic fields is small relative to the depth of the surface. These are sufficient approximations for a wide range of applications in domestic induction heating [1].

The second geometry considered is the general multilayered problem, where  $N + 1$  distinct layers of homogenous magnetic permeability and conductivity are stacked on top of one another in the  $\hat{z}$  direction. The excitation currents can either be placed above the entire stack or sandwiched in between specific layers. This general arrangement embodies the cases where the depth of penetration through at least one of the layers is comparable to the thickness of that layer, and that the heated surface can no longer be considered to be semi-infinite in its depth. For domestic induction heating, the multilayered problem is applicable when a non-ferromagnetic material (e.g. aluminum or copper) is heated.

In both cases, it is important to note that the multilayered Green's function is dyadic, and that it is expressed as a tensor field rather than a vector or a scalar field. This reflects the fact that for each component of the current density vector  $\mathbf{J}$ , cross-coupling can occur, causing the resultant  $\mathbf{A}$  field to have components in all three dimensions. The dyadic Green's function is often written using the tensor notation:

$$\overline{\overline{\mathbf{G}}} = \begin{bmatrix} \mathbf{G}_x & \mathbf{G}_y & \mathbf{G}_z \end{bmatrix} = \begin{bmatrix} G_{xx} & G_{xy} & G_{xz} \\ G_{yx} & G_{yy} & G_{yz} \\ G_{zx} & G_{zy} & G_{zz} \end{bmatrix} \quad (3.8)$$

such that  $G_{jk}$  is the Green's function contribution of a current in the  $k$  direction to

the magnetic potential vector in the  $j$  direction. The Green's function convolution integral is then rewritten as a dot product equation in the following form:

$$\mathbf{A}(x, y, z) = \int_C I(x, y, z) \overline{\overline{\mathbf{G}}}(x, y, z) \cdot d\mathbf{s} \quad (3.9)$$

where  $d\mathbf{s}$  is the line integral vector,  $C$  is the contour of the conductor and  $I(x, y, z)$  is the magnitude of the current at that point.

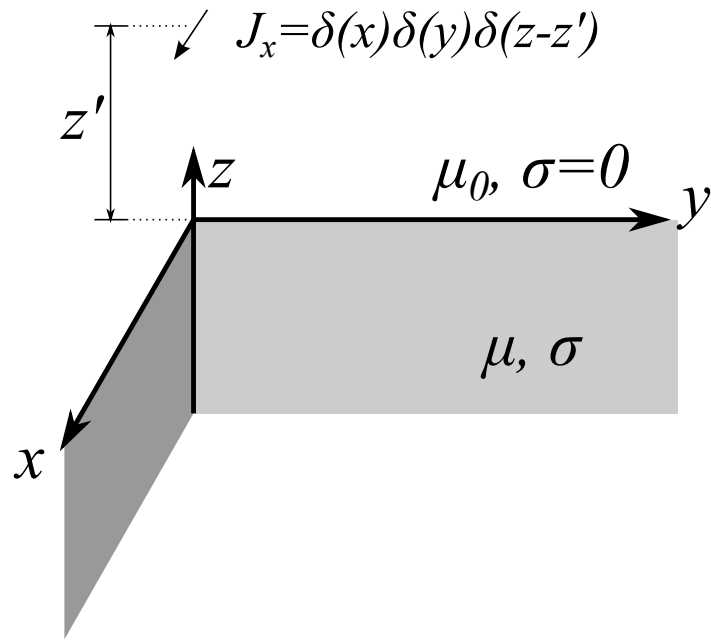
### 3.2.1 The Dyadic Green's Function for the Semi-Infinite Half-Space

The arrangement of a transverse point current source above a single semi-infinite surface is shown in Figure 3-1. The Green's function for this system has been extensively studied since the earliest days of induction heating, and for this reason its derivation will not be repeated here. For a current source located at  $(0, 0, z')$ , the  $\hat{x}$  component of the magnetic potential vector  $A$  in free-space is the following [43]:

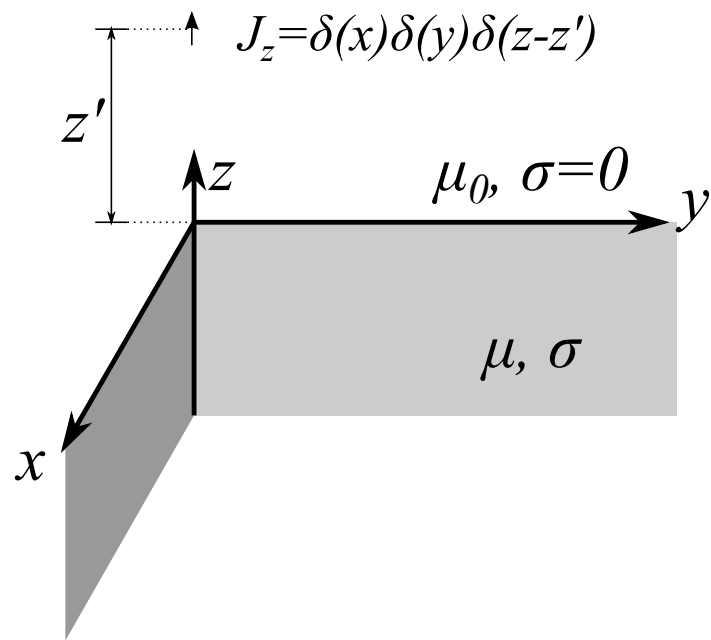
$$G_{xx}(r, z) = \frac{\mu_0 I}{4\pi} \left( \frac{1}{\sqrt{r^2 + (z - z')^2}} + \frac{1}{\sqrt{r^2 + (z + z')^2}} + \int_0^\infty \frac{-2\eta}{\mu_r \gamma + \eta} e^{-\gamma(z+z')} J_0(\gamma r) d\gamma \right) \quad (3.10)$$

with  $\eta^2 = \gamma^2 + j\omega\mu_r\mu_0\sigma$ . Note that the first term in this expression is the  $1/r$  free-space Green's function of the original current source at  $z = d$ , and the second term is the free-space Green's function of the reflected current source at  $z = -d$ . The second and third terms characterize the response of the conductive half-space upon the point current source. Noting the rotational symmetry of the system and assuming isotropy in the material,  $G_{yy}(r, z) = G_{xx}(r, z)$ , and no cross-coupling occurs when current is excited in the transverse direction.

The derivation for the perpendicular point current source is more complicated. An analysis of Transverse-Electric and Transverse-Magnetic propagation modes by Bowler [44] using the second-order magnetic potentials showed that the interface between free-space and the conductor perfectly reflects the perpendicular magnetic vector potential  $A_z$ , as if it were a perfect conductor. This means that for a perpen-



(a)



(b)

Figure 3-1: Geometries of the point current source above a semi-infinite surface: (a) Transverse system; (b) Perpendicular system.

dicular source at  $(0, 0, z')$ :

$$G_{zz}(r, z) = \frac{\mu_0 I}{4\pi} \left[ \frac{1}{\sqrt{r^2 + (z - z')^2}} + \frac{1}{\sqrt{r^2 + (z + z')^2}} \right] \quad (3.11)$$

However, in the perpendicular mode of excitation, some energy is cross-coupled to the radial direction. Juillard *et al.* derived this Green's function to be [43]:

$$G_{rz}(r, z) = \frac{\mu_r \mu_0 I}{2\pi} \int_0^\infty \frac{\gamma}{\mu_r \gamma + \eta} e^{-\gamma(z+z')} J_1(\gamma r) d\gamma \quad (3.12)$$

The Cartesian Green's functions  $G_{xz}(r, z)$  and  $G_{yz}(r, z)$  can be retrieved by the substitution  $\hat{r} = (x - x')/\|\mathbf{r} - \mathbf{r}'\|\hat{x} + (y - y')/\|\mathbf{r} - \mathbf{r}'\|\hat{y}$ . Thus the overall Green's function tensor can be written as:

$$\overline{\overline{G}}(\mathbf{r}, \mathbf{r}') = \begin{bmatrix} G_{xx}(\mathbf{r}, \mathbf{r}') & 0 & 0 \\ 0 & G_{xx}(\mathbf{r}, \mathbf{r}') & 0 \\ \frac{|x-x'|}{\sqrt{(x-x')^2+(y-y')^2}} G_{rz}(\mathbf{r}, \mathbf{r}') & \frac{|y-y'|}{\sqrt{(x-x')^2+(y-y')^2}} G_{rz}(\mathbf{r}, \mathbf{r}') & G_{zz}(\mathbf{r}, \mathbf{r}') \end{bmatrix} \quad (3.13)$$

It is important to note that for each Green's function, the quasistatic condition  $\nabla \cdot \mathbf{E} = -j\omega \nabla \cdot \mathbf{A} = 0$  does not hold, because the current filament does not constitute a closed loop. Thus for these equations to have any physical significance,  $\nabla \cdot \mathbf{A} = 0$  must be explicitly enforced once the loop is closed. First, consider a closed loop convolution integral along some contour with the dyadic Green's function.

$$\mathbf{A}(\mathbf{r}) = \oint \overline{\overline{G}}(\mathbf{r}, \mathbf{r}') \cdot d\mathbf{s} = \oint \overline{\overline{G}}(\mathbf{r}, \mathbf{r}') \cdot \hat{t} dl \quad (3.14)$$

$\mathbf{A}(\mathbf{r})$  denotes the magnetic vector potential of the final closed loop measured at the field point  $\mathbf{r}$ . The integration is performed with  $d\mathbf{s}$  along the along the  $\mathbf{r}' = (x', y', z')$  source point coordinates. The tensor dot product can be broken up into its three components:

$$\mathbf{A} = \oint G_{xx} \hat{x} (\hat{x} \cdot \hat{t}) dl + \oint G_{yy} \hat{y} (\hat{y} \cdot \hat{t}) dl + \oint \mathbf{G}_z (\hat{z} \cdot \hat{t}) dl \quad (3.15)$$

Note that only  $G_{xx}$  and  $G_{yy}$  of the vectors  $\mathbf{G}_x$  and  $\mathbf{G}_y$  are non-zero, because cross-coupling does not occur in the transverse direction. The divergence of this expression

is:

$$\begin{aligned}\nabla \cdot \mathbf{A} &= \oint \frac{\delta}{\delta x} G_{xx} (\hat{x} \cdot \hat{t}) dl + \oint \frac{\delta}{\delta y} G_{xx} \hat{y} (\hat{y} \cdot \hat{t}) dl \\ &\quad + \oint (\nabla \cdot \mathbf{G}_z) (\hat{z} \cdot \hat{t}) dl\end{aligned}\quad (3.16)$$

To ensure that the closed loop divergence is zero, the line integral on the right hand side of (3.16) must evaluate to zero. By the fundamental theorem of calculus, this is guaranteed if the integrand of (3.16) can be expressed as a gradient vector field with respect to the variables of integration, that is the source variables  $x', y', z'$ . As it currently stands, (3.16) can be written as the line integral around the vector field  $\mathbf{F}$ :

$$\nabla \cdot \mathbf{A} = \oint \mathbf{F} \cdot d\mathbf{s} \quad (3.17)$$

where

$$\mathbf{F} = \begin{pmatrix} \frac{\delta}{\delta x} G_{xx} \\ \frac{\delta}{\delta y} G_{xx} \\ \nabla \cdot \mathbf{G}_z \end{pmatrix} \quad (3.18)$$

To show that  $\mathbf{F}$  is a gradient field with respect to the source variables, note that in the transverse directions,  $G_{xx}$  has a dependence on  $(r - r')$ . Because of this,

$$\frac{\delta}{\delta x} G_{xx} = -\frac{\delta}{\delta x'} G_{xx}, \quad \frac{\delta}{\delta y} G_{xx} = -\frac{\delta}{\delta y'} G_{xx} \quad (3.19)$$

and

$$\mathbf{F} = \begin{pmatrix} -\frac{\delta}{\delta x'} G_{xx} \\ -\frac{\delta}{\delta y'} G_{xx} \\ \nabla \cdot \mathbf{G}_z \end{pmatrix} \quad (3.20)$$

If the following gauge condition is imposed:

$$\nabla \cdot \mathbf{G}_z = -\frac{\delta}{\delta z'} G_{xx} \quad (3.21)$$

then

$$\mathbf{F} = -\nabla' G_{xx} \quad (3.22)$$

where  $\nabla'$  is the del operator with respect to the source variables  $x', y', z'$ . Since  $G_{xx}$  is smooth and continuous due to the boundary conditions imposed on it,  $\mathbf{F}$  is a conservative gradient field, and the closed loop line integral around  $\mathbf{F}$  by  $d\mathbf{s}$  traversing as the vector  $\mathbf{r}'$  must sum to zero. Thus as it is shown,  $\nabla \cdot \mathbf{A} = 0$  is guaranteed if the

gauge condition in (3.21) is satisfied. One can verify that this is indeed the case for (3.11) and (3.12).

### 3.2.2 The Dyadic Green's function Multiple-Layered Configuration

Preliminary work on multiple-layered conductors were first conducted in the earliest days of eddy current analysis by Dodds and Deeds in 1968, with their derivation of the equations for the two-layered conductor [6]. A particularly interesting geometry for the purpose of induction heating is known as the “sandwich” configuration, where the coil is placed between two conductive materials. Derivations for a circular coil placed within specific sandwich arrangements were presented by Hurley *et al.* [25]. These expressions were adapted by Acero *et al.* for the induction heating application [45], and developed into generalized expressions for all multilayered configurations [12].

#### Transverse Component

Consider the multilayered system in Figure 3-2. The system is arranged with each of the multiple layers stretched infinitely along the  $\hat{x}$  and  $\hat{y}$  axes, with depth in the  $\hat{z}$  direction. For mathematical convenience, the boundary for the first, top layer starts at  $z = 0$ , and each subsequent layer boundary is located at  $z = d_i$  where  $d_i$  relates to the deepest edge of layer  $i$ . Noting the rotational symmetry, the Hankel transform can be taken along the radial dimension:

$$A_i(r, z) = \int_0^\infty A_i^*(k, z) k J_0(kr) dk \quad (3.23)$$

The transformed variables  $A_i^*$  can be placed into the diffusion equation to result in a general expression for  $A_i^*$ :

$$A_i^* = \begin{cases} B_i \sinh(\eta_i(z - d_i)) + C_i \cosh(\eta_i(z - d_i)) & i \in 1 \dots N - 1 \\ C_0 e^{-\eta_0 z} & i = 0 \\ C_N e^{\eta_N(z + d_N)} & i = N \end{cases} \quad (3.24)$$

where  $\eta_i^2 = k^2 + j\omega\mu_i\sigma_i$ . The magnetic field in the  $\hat{y}$  direction  $H_y$  has the following

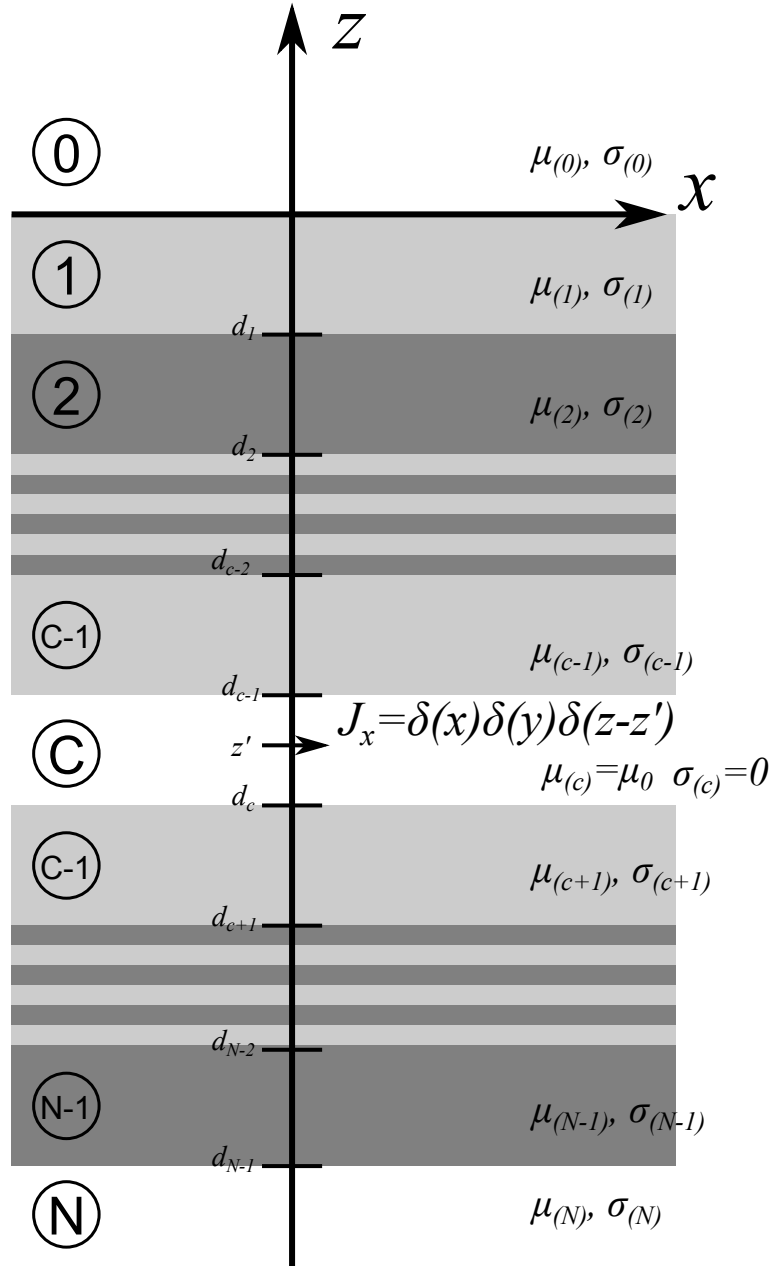


Figure 3-2: Geometry of the point current source within the multilayered configuration

values:

$$H_i^* = \begin{cases} B_i \lambda_i \cosh(\eta_i(z - d_i)) + C_i \lambda_i \sinh(\eta_i(z - d_i)) & i \in 1 \dots N - 1 \\ -C_0 \lambda_0 e^{-\eta_0 z} & i = 0 \\ C_N \lambda_N e^{\eta_N(z + d_N)} & i = N \end{cases} \quad (3.25)$$

where  $\lambda_i = \eta_i / \mu_i$ . The middle layers will require boundary matching. At the bottom of each middle layer ( $i \in 1 \dots N - 1$ ) where  $z = d_i$ :

$$A_i^* = C_i, \quad H_i^* = B_i \lambda_i \quad (3.26)$$

At the top of each middle layer where  $z = d_{i-1}$ :

$$A_i^* = B_i \sinh(\eta_i t_i) + C_i \cosh(\eta_i t_i) \quad (3.27)$$

$$H_i^* = B_i \lambda_i \cosh(\eta_i t_i) + C_i \lambda_i \sinh(\eta_i t_i) \quad (3.28)$$

where  $t_i$  is the depth of layer  $i$ :  $t_i = d_i - d_{i-1}$ . Let both  $A_i^*$  and  $H_i^*$  be continuous along each middle boundary:

$$\begin{bmatrix} \frac{\lambda_{i+1}}{\lambda_i} \cosh(\eta_{i+1} t_{i+1}) & \frac{\lambda_{i+1}}{\lambda_i} \sinh(\eta_{i+1} t_{i+1}) \\ \sinh(\eta_{i+1} t_{i+1}) & \cosh(\eta_{i+1} t_{i+1}) \end{bmatrix} \begin{pmatrix} B_{i+1} \\ C_{i+1} \end{pmatrix} = \begin{pmatrix} B_i \\ C_i \end{pmatrix} \quad (3.29)$$

Let us denote this matrix as  $\overline{\overline{M}}_{i+1}$ . Note that the matrix is easily inverted:

$$\begin{bmatrix} \frac{\lambda_i}{\lambda_{i+1}} \cosh(\eta_{i+1} t_{i+1}) & -\sinh(\eta_{i+1} t_{i+1}) \\ -\frac{\lambda_i}{\lambda_{i+1}} \sinh(\eta_{i+1} t_{i+1}) & \cosh(\eta_{i+1} t_{i+1}) \end{bmatrix} \begin{pmatrix} B_i \\ C_i \end{pmatrix} = \begin{pmatrix} B_{i+1} \\ C_{i+1} \end{pmatrix} \quad (3.30)$$

Now, consider a transverse current filament of current  $I$  in layer  $c$ , at the depth of  $z = z'$ . Furthermore, let this layer be free-space. This filament changes the boundary conditions at the top and bottom of layer  $c$  to be respectively:

$$A_c^*(z = d_{c-1}) = B_c \sinh(kt_c) + C_c \cosh(kt_c) + \frac{\mu_0 I}{4\pi k} e^{-k(d_{c-1} - z')} \quad (3.31)$$

$$H_c^*(z = d_{c-1}) = B_c \frac{k}{\mu_0} \cosh(kt_c) + C_c \frac{k}{\mu_0} \sinh(kt_c) - \frac{I}{4\pi} e^{-k(d_{c-1} - z')} \quad (3.32)$$

$$A_c^*(z = d_c) = C_c + \frac{\mu_0 I}{4\pi k} e^{-k(d_c + z')} \quad (3.33)$$

$$H_c^*(z = d_c) = B_c \frac{k}{\mu_0} + \frac{I}{4\pi} e^{-k(d_c + z')} \quad (3.34)$$



with  $\overline{\overline{M}}_i$  defined according to (3.29), and:

$$\Gamma_i = \begin{pmatrix} B_i \\ C_i \end{pmatrix} \quad (3.40)$$

$$\overline{\overline{C}} = \begin{bmatrix} 1 & \frac{2\Phi}{e^{2\eta_1 t_1} + \Phi} \end{bmatrix} \quad (3.41)$$

$$\overline{\overline{D}} = \begin{bmatrix} \frac{\lambda_{N-1}}{\lambda_N} & -1 \end{bmatrix} \quad (3.42)$$

$$F_c = \begin{pmatrix} \frac{k}{\mu_0 \lambda_{c-1}} \\ -1 \end{pmatrix} \frac{\mu_0 I}{4\pi k} e^{-k(d_{c-1}-z')} \quad (3.43)$$

$$F_{c+1} = \begin{pmatrix} 1 \\ 1 \end{pmatrix} \frac{\mu_0 I}{4\pi k} e^{-k(d_c+z')} \quad (3.44)$$

A number of matrix inversion technique can then be applied to solve for all unknown coefficients in the system. Once  $B_c$  and  $C_c$  are calculated from the matrix equation system, the Green's function in the coil layer  $c$  can be written as:

$$G_{xx.c}(r, z) = A_c(r, z) = \frac{\mu_0 I}{4\pi} \frac{1}{\sqrt{r^2 + (z - z')^2}} + \int_0^\infty [B_c \sinh(k(z - d_c)) + C_c \cosh(k(z - d_c))] k J_0(kr) dk \quad (3.45)$$

In practice, both  $B_c$  and  $C_c$  are dependent upon  $k$ , and the matrix equation can only be numerically solved for a single  $k$  value. In the interest of computational speed, it is necessary to tabulate the Green's function with respect to  $r$ ,  $z$  and  $z'$ , rather than to calculate it on-the-fly. Note that while (3.45) is similar in appearance to previous works [12], its advantage is that the  $1/r$  free-space Green's function is explicitly isolated during the formulation stage.

## Perpendicular Component

The derivation for the perpendicular component of the multilayer Green's function extends the half-space derivation in Section 3.2.1. Here, the  $\mathbf{H}$  field generated by a perpendicular current filament in the multilayered configuration exists only in the  $\hat{\phi}$  direction, due to the cylindrical symmetry of the system and the orthogonality imposed by the definition of the magnetic potential vector and the diffusion equation. Because of this,  $\mathbf{A}$  exists only in the  $\hat{r}$  and  $\hat{z}$  directions, and does not have any value or any dependence along  $\phi$ .

First, as shown in the case for the semi-infinite half-plane by Bowler [44],  $A_z = 0$  is enforced within all the regions except the source region. This means for a coil

placed in layer  $c$  at a depth of  $z'$ :

$$A_{z,i}^* = \begin{cases} \frac{\mu_0 I}{4\pi k} e^{-k|z-z'|} + D_c \sinh(k(z-d_c)) + F_c \cosh(k(z-d_c)) & i = c \\ 0 & i \neq c \end{cases} \quad (3.46)$$

The radial component is treated in a similar way to how it was treated in the transverse case, but is now transformed with the first-order Hankel transform:

$$A_{ri}^* = \begin{cases} B_i \sinh(\eta_i(z-d_i)) + C_i \cosh(\eta_i(z-d_i)) & i \in 1 \dots N-1 \\ C_0 e^{-\eta_0 z} & i = 0 \\ C_N e^{\eta_N(z+d_N)} & i = N \end{cases} \quad (3.47)$$

The radial magnetic field  $H_r = \frac{1}{\mu} (\frac{\delta}{\delta r} A_z - \frac{\delta}{\delta z} A_r)$ . Noting that  $\frac{\delta}{\delta r} J_0(kr) = -kJ_1(kr)$  and keeping the same definition of  $\lambda_i$  from before:

$$H_{ri}^* = \begin{cases} -B_i \lambda_i \cosh(\eta_i(z-d_i)) - C_i \lambda_i \sinh(\eta_i(z-d_i)) & i \in 1 \dots N-1, i \neq c \\ C_0 \lambda_0 e^{-\eta_0 z} & i = 0 \\ -C_N \lambda_N e^{\eta_N(z+d_N)} & i = N \end{cases} \quad (3.48)$$

It is clear from these sets of equations that the boundary matching matrix  $\overline{\overline{M}}_{i+1}$  would be the same as in the transverse current case. This makes sense physically because only the transverse  $\mathbf{A}$  and  $\mathbf{H}$  fields are matched in either cases. However,  $H_r$  is more complicated than the transverse case at the layer containing the coil:

$$H_{rc}^* = -\lambda_c \left[ \frac{\mu_0 I}{4\pi k} e^{-k|z-z'|} + D_c \cosh(k(z-d_c)) + F_c \sinh(k(z-d_c)) + B_c \cosh(\eta_c(z-d_c)) + C_c \sinh(\eta_c(z-d_c)) \right] \quad (3.49)$$

The following conditions result from (3.46) and (3.49) at the coil layer boundaries:

$$\overline{\overline{M}}_{c+1} \begin{pmatrix} B_{c+1} \\ C_{c+1} \end{pmatrix} = \begin{pmatrix} B_c \\ C_c \end{pmatrix} + \begin{pmatrix} 1 \\ 0 \end{pmatrix} \left[ D_c + \frac{\mu_0 I}{4\pi k} e^{-k(d_c+z')} \right] \quad (3.50)$$



functions are:

$$G_{zz.c}(r, z) = \frac{\mu_0 I}{4\pi} \frac{1}{\sqrt{r^2 + (z - z')^2}} + \int_0^\infty [D_c \sinh(k(z - d_c)) + F_c \cosh(k(z - d_c))] k J_0(kr) dk \quad (3.56)$$

and

$$G_{rz.c}(r, z) = \int_0^\infty [B_c \sinh(k(z - d_c)) + C_c \cosh(k(z - d_c))] k J_1(kr) dk \quad (3.57)$$

### 3.2.3 Application of Numerical Hankel Transforms

Due to the inherent radial symmetry for the planar-symmetric geometry, all of the Green's functions above can be expressed as Hankel transform integrals, where the Hankel transform is defined to be

$$F(k) = \mathcal{H}_\nu [f(r)] = \int_0^\infty f(r) J_\nu(kr) r dr \quad (3.58)$$

$$f(r) = \mathcal{H}_\nu^{-1} [F(k)] = \int_0^\infty F(k) J_\nu(kr) k dk \quad (3.59)$$

Here,  $J_\nu$  is the order  $\nu$  Bessel function of the first kind. This integral is challenging for most numerical quadrature algorithms, due to the oscillating kernel of the integral and the unbounded integration domain. Fortunately, there exist a variety of algorithms designed to numerically evaluate the Hankel transform integral with a single transformation operation for a set of  $r$  values. The use of these specialized algorithms greatly accelerates the computation of the Green's functions.

Two important algorithms considered here are the Quasi-Fast Hankel Transform (QFHT) by Siegman [46] and the Quasi-Discrete Hankel Transform (QDHT) by Guizar-Sicairos and Gutierrez-Vega [47]. While other algorithms exist, such as the High-accuracy Fast Hankel Transform (HAFHT) [48] and various back projection and slice projection methods [49], these two algorithms stand out as the benchmark used in literature due to their high performance and ease of implementation. Both were included as components of the model, although empirically the QDHT was found to be better performing.

#### Quasi-Fast Hankel Transform

The Quasi-Fast Hankel transform (QFHT) [46] characterizes an entire family of important algorithms where the variables  $r$  and  $k$  from (3.58),(3.59) are discretely sam-

pled according to an exponential pattern:

$$r_m = r_o e^{\alpha m}, \quad k_n = k_o e^{\alpha n} \quad (3.60)$$

Here,  $\alpha$  is a common scaling factor shared between the two variables. By substituting the exponentially sampled discrete  $r_m$  and  $k_n$  into the Hankel transform and discretizing, the Hankel transform is simplified to a discrete cross-correlation relation. The cross-correlation can then be rapidly evaluated using the fast Fourier transform algorithm.

The QFHT and other exponentially sampled algorithms are widely praised for their  $\mathcal{O}[N \log N]$  speed and their efficient use of memory [49]. Unfortunately, the use of exponential sampling is often inconvenient, and the interpolation, quadrature or resampling scheme required to rectify this adds an additional layer of computation time and loss of accuracy. Moreover, it is often difficult to control the error size of the algorithm, because it is influenced by the arbitrary parameters  $r_o$ ,  $k_o$  and  $\alpha$  in addition to the number of terms used to evaluate the transform.

### Quasi-Discrete Hankel Transform

The Quasi-Discrete Hankel Transform (QDHT) is an algorithm first developed for the zeroth order Hankel transform by Yu *et al.* [50], and later on extended to integer order Hankel transforms by Guizar-Sicairos and Gutierrez-Vega [47]. The algorithm is based on using a closed-form approximation of the transform equations (3.58), (3.59) at the roots of the Bessel functions of the first kind. Addressing many issues of the QFHT, the QDHT algorithm produces a uniformly sample output, and with its accuracy controlled only by the number of samples used. However, it is also considerably slower and more storage intensive, because the actual transformation is performed with an  $\mathcal{O}[N^2]$  matrix multiplication.

## 3.3 Evaluation of the Modified Green's Function via Quadrature

As explained in Section 3.1, the dyadic Green's function of a point current source within a multilayered system can be decomposed into two components: the free-space Green's function due to the point current source itself, and the modified Green's function due to the eddy currents and magnetic domains of the rest of the system.

While several closed form solutions to the free-space Green’s function have been derived, the modified Green’s function must be numerically integrated to obtain the response of the conductive magnetic surface.

The challenge of the task lies in the need to integrate over several dimensions: the interaction between two finite-volume conductors will require integration over six dimensions (twice for each cartesian dimension) [16]. Conventional numerical integration algorithms are bound by the “curse of dimensionality”, because the cost of such an operation grows at an exponential rate, to the point of being impractical once more than two or three dimensions are considered. This issue of dimensionality was identified as an overwhelming challenge by previous authors [37].

Fortunately, over the past two decade, several numerical integration schemes have been developed that can overcome the curse of dimensionality:

- Smolyak’s construction, also known in literature as the blending method, the boolean method, or the sparse grid method. In this approach, multidimensional quadrature formulas are constructed from the tensor products of a suitable one-dimensional quadrature formula. [51]
- Lattice Methods, a simple and mathematically elegant technique, based on the generalizations of the rectangle rule, for integrating smooth, periodic functions over many dimensions. Non-periodic functions can too be integrated by lattice methods when a nonlinear transformation is used before the quadrature [52].
- Monte Carlo and deterministic Monte Carlo techniques, based on probabilistic techniques [53].
- Adaptive subdivision rules, that intelligently allocates quadrature points to each dimension according to its importance [54, 55].

Each one of these schemes is developed to be efficient for a specific set of problem, for which it can then evaluate with logarithmic growth of costs with increasing dimensionality.

The quadrature scheme used within this thesis is a sparse grid formulation by Heiss and Winschel [56]. Compared to the other options, the sparse grid formulation is the fastest performing quadrature scheme of the options available, being a single process involving only function evaluations and multiplication. However, the ability to estimate and control the quadrature within a certain error tolerance is lost. Given the smoothness of the modified Green’s function with the singularity removed, this was deemed to be an acceptable price to pay.

In the version of the quadrature used, the standard Gauss-Legendre quadrature is used for the base one-dimensional quadrature scheme, and it is extended to higher dimensions using Smolyak's combination of tensor products. The integration over a hypercube of many dimensions is then approximated as a series of weights and function evaluations at specific points. For example, a six-dimensional integration over the hypercube  $\Omega = [0, 1]^6$  is approximated with a six-dimensional quadrature scheme:

$$\int_{\Omega} f(x, y, z, x', y', z') d\{x, y, z, x', y', z'\} \approx \sum_{j=0}^N w_j f(\mathbf{p}_j) \quad (3.61)$$

where  $w_j$  is a series of weights and  $\mathbf{p}_j$  is a series of evaluation points. The supplemental code library supplied by Heiss and Winschel was used to generate the weights and evaluation points.

### Filament to filament interaction

The partial mutual inductance contribution can be calculated by integrating the electric field generated by one filament with the remainder of the Green's function along the contour of another. Using the modified multilayered dyadic Green's function  $\overline{\overline{G}}$ , the field generated by filament 1 in the  $\hat{x}$  direction can be expressed in tensor dot product form as:

$$\mathbf{E}_k(\mathbf{r}) = j\omega I \int_{b_k}^{c_k} \overline{\overline{G}}(\mathbf{r}, \mathbf{r}') \cdot d\mathbf{l}_1$$

Integrating the electric field along the contour of filament 1, and dividing by the current flowing through conductor 1 and  $j\omega$  yields the mutual inductance  $M$ :

$$M = \int_{b_k}^{c_k} \int_{b_m}^{c_m} \overline{\overline{G}}(\mathbf{r}, \mathbf{r}') \cdot d\mathbf{l}_1 \cdot d\mathbf{l}_2 \quad (3.62)$$

$$M = \int_{b_k}^{c_k} \int_{b_m}^{c_m} \overline{\overline{G}}(\mathbf{r}, \mathbf{r}') \cdot \hat{t}_1 \cdot \hat{t}_2 dl_1 dl_2 \quad (3.63)$$

The paths of integration are:

$$\mathbf{r}' = \mathbf{s}_1 + l_1 \hat{t}_1 \quad (3.64)$$

$$\mathbf{r} = \mathbf{s}_2 + l_2 \hat{t}_2 \quad (3.65)$$

where  $\mathbf{s}_1$  and  $\mathbf{s}_2$  are the starting points and  $\hat{t}_1$  and  $\hat{t}_2$  are the unit vectors pointing

tangentially along the lengths of each filament. To resolve the anisotropy of the dyadic Green's function, let us define a new unit vector,  $\hat{T}$  as the normalized projection of  $\hat{t}_1$  to the transverse plane:

$$\hat{T} = \frac{(\hat{t}_1 \cdot \hat{x})\hat{x} + (\hat{t}_1 \cdot \hat{y})\hat{y}}{\sqrt{(\hat{t}_1 \cdot \hat{x})^2 + (\hat{t}_1 \cdot \hat{y})^2}} \quad (3.66)$$

With this,  $\hat{t}_1$  can be broken down into its transverse and perpendicular components:

$$\hat{t}_1 = (\hat{t}_1 \cdot \hat{T})\hat{T} + (\hat{t}_1 \cdot \hat{z})\hat{z} \quad (3.67)$$

The  $\hat{T}$  component of  $\hat{t}_1$  generates a field purely in the  $\hat{T}$  direction. The portion of this field that is coupled to the second conductor is equal to  $(\hat{t}_2 \cdot \hat{T})$ . Thus:

$$M_T = (\hat{t}_1 \cdot \hat{T})(\hat{t}_2 \cdot \hat{T}) \int_0^{L_1} \int_0^{L_2} G_{xx}(\mathbf{r}, \mathbf{r}') dl_1 dl_2 \quad (3.68)$$

The  $\hat{z}$  component of  $\hat{t}_1$  generates two orthogonal fields, one in the  $\hat{z}$  direction and one in the transverse radial direction  $\hat{r}$  from the source point to the field point. Describing the components as interactions in three dimensions:

$$M_{zz} = (\hat{t}_1 \cdot \hat{z})(\hat{t}_2 \cdot \hat{z}) \int_0^{L_1} \int_0^{L_2} G_{zz}(\mathbf{r}, \mathbf{r}') dl_1 dl_2 \quad (3.69)$$

$$M_{rz} = \int_0^{L_1} \int_0^{L_2} \frac{(\hat{t}_2 \cdot \hat{x})|x - x'| + (\hat{t}_2 \cdot \hat{y})|y - y'|}{\sqrt{(x - x')^2 + (y - y')^2}} G_{rz}(\mathbf{r}, \mathbf{r}') dl_1 dl_2 \quad (3.70)$$

The total mutual inductance is the sum of these orthogonal components,  $M = M_T + M_{zz} + M_{rz}$ .

## Conductor to conductor interaction

The filament approximation used to derive these analytical solutions also introduces errors, because real conductors have finite cross-sections that also contribute fields towards the fields of the system. This effect is well understood if the current density is assumed to be constant throughout the conductor. The Geometric Mean Distance (GMD) method can be used to calculate correction factors to compensate for the errors introduced by the filament approximation [31, 57]. With circular cross sections, the filament approximation is said to be accurate to about 15 parts in 1000 without the need for a correction factor [31]. The constant current density assumption is

generally valid for a wide range of frequencies if the coil is wound with litz wires.

As the volume of the filaments increases in proportion to their relative distances, the cross-sectional areas can no longer be ignored. In this case, the average mutual impedance over the cross-sectional areas of the conductors can be taken to extend the zero-volume results to the finite-volume conductor. For this to be applicable, two assumptions must hold: (1) current flows only in the direction along the length of the conductor; (2) current density is uniform within the conductor.

To perform this averaging over the cross-sectional areas of both conductors, consider extending the definition of  $\mathbf{r}$  and  $\mathbf{r}'$  from (3.64) and (3.65) with two additional components in orthogonal directions:

$$\mathbf{r}' = \mathbf{s}_1 + l_1 \hat{t}_1 + w_1 \hat{w}_1 + h_1 \hat{h}_1 \quad (3.71)$$

$$\mathbf{r} = \mathbf{s}_2 + l_2 \hat{t}_2 + w_2 \hat{w}_2 + h_2 \hat{h}_2 \quad (3.72)$$

where  $\hat{w}_j$  and  $\hat{h}_j$  are the unit vectors pointing along the widths and heights of each filament. Extending (3.68), the transverse component can now be written as:

$$M_T = \frac{(\hat{t}_1 \cdot \hat{T})(\hat{t}_2 \cdot \hat{T})}{W_1 W_2 H_1 H_2} \int_0^{L_1} \int_0^{L_2} \int_0^{W_1} \int_0^{W_2} \int_0^{H_1} \int_0^{H_2} G_{xx}(\mathbf{r}, \mathbf{r}') d\{l_1, l_2, w_1, w_2, h_1, h_2\} \quad (3.73)$$

Similarly averaging over the cross-sectional areas in (3.69) and (3.70):

$$M_{zz} = \frac{(\hat{t}_1 \cdot \hat{z})(\hat{t}_2 \cdot \hat{z})}{W_1 W_2 H_1 H_2} \int_0^{L_1} \int_0^{L_2} \int_0^{W_1} \int_0^{W_2} \int_0^{H_1} \int_0^{H_2} G_{zz}(\mathbf{r}, \mathbf{r}') d\{l_1, l_2, w_1, w_2, h_1, h_2\} \quad (3.74)$$

$$M_{rz} = \frac{1}{W_1 W_2 H_1 H_2} \int_0^{L_1} \int_0^{L_2} \int_0^{W_1} \int_0^{W_2} \int_0^{H_1} \int_0^{H_2} \frac{(\hat{t}_2 \cdot \hat{x})|x - x'| + (\hat{t}_2 \cdot \hat{y})|y - y'|}{\sqrt{(x - x')^2 + (y - y')^2}} \cdot G_{rz}(\mathbf{r}, \mathbf{r}') d\{l_1, l_2, w_1, w_2, h_1, h_2\} \quad (3.75)$$

As before, the total mutual inductance is the sum of these orthogonal components,  $M = M_T + M_{zz} + M_{rz}$ .

### 3.4 Eddy Current Loss Profile

In order to determine the heating profile and temperature profile of the heated load, the field model must also evaluate the eddy current loss profile within the conductive, magnetic media. As an integral formulation method, the PEEC model only solves for the currents flowing through the filaments. In order to obtain the field strength within

the domain, the Green's function must be convolved with the evaluated boundary values at specific observation points.

### 3.4.1 Theoretical Basis

By the Poynting theorem, the complex power crossing the  $z = 0$  interface from the  $z > 0$  region can be described by the time-averaged Poynting's vector in the  $\hat{z}$  direction along this plane:

$$S = \int_{surface} \frac{1}{2} (\mathbf{E} \times \mathbf{H}^*) \cdot (-\hat{z}) da \quad (3.76)$$

where the asterisk here denotes the complex conjugate. If the bounds of the integration are extended to infinity then the fields on the side of the box are reduced to zero. The only non-zero integration surface is  $z = 0$ . Applying the divergence theorem, the identity  $\nabla \cdot (\mathbf{E} \times \mathbf{H}^*) = (\nabla \times \mathbf{E}) \cdot \mathbf{H}^* - (\nabla \times \mathbf{H}^*) \cdot \mathbf{E}$  and the standard constitutive relations:

$$S = \frac{j\omega}{2\mu} \int_V \|\mathbf{B}\|^2 dV + \frac{\sigma}{2} \int_V \|\mathbf{E}\|^2 dV \quad (3.77)$$

where the volume  $V$  corresponds to the conductive  $z < 0$  region. The first term here corresponds to the magnetic storage of energy, and the second term corresponds to eddy losses in the load. Due to the MQS approximation in place, the electric field stores no energy.

Most induction heating loads have magnetic permeabilities of  $\mu_r \gg 1$ . Because of this, their refractive indices are very high and the internal electromagnetic waves within them are approximately plane waves propagating in the  $-\hat{z}$  direction. Under these conditions, transverse power flow is negligible to perpendicular power flow, and:

$$\frac{1}{2} (\mathbf{E} \times \mathbf{H}^*) \cdot (-\hat{z}) = \frac{j\omega}{2\mu} \int_0^{-\infty} \|\mathbf{B}\|^2 dz + \frac{\sigma}{2} \int_0^{-\infty} \|\mathbf{E}\|^2 dz \quad (3.78)$$

The absence of tangential power flow beneath the interaction surface is an important assumption for our formulation to hold. Consider the scalar field  $P$ , defined as the real component of the Poynting vector:

$$P = \Re \left\{ \frac{1}{2} (\mathbf{E} \times \mathbf{H}^*) \cdot (-\hat{z}) \right\} \quad (3.79)$$

such that  $\iint P da = \Re \{S\}$ . If tangential power flow is negligible, then  $P$  can be used directly as the heating profile over the surface of the load.

The use of the Poynting vector is well-established in induction heating for the semi-infinite half-plane configuration discussed previously in Section 3.2.1. With a homogenous and isotropic eddy current media, it can be shown that all fields decay at a rate of the skin depth  $\delta = \sqrt{2/(\omega\mu\sigma)}$ . With this,  $P$  becomes the classic surface resistance relation:

$$P = \frac{1}{2\sigma\delta} (\|\mathbf{H}_x(z=0)\|^2 + \|\mathbf{H}_y(z=0)\|^2)$$

For generality however, it is necessary to obtain a relation for  $P$  that will work on heated loads conductors of all thickness and layer compositions. Noting that  $A_z$  is approximately zero for a mostly planar coil system, (3.79) simplifies to:

$$P = -\frac{\omega}{2\mu} \Im \left\{ A_x \left( \frac{\delta A_x^*}{\delta z} \right) + A_y \left( \frac{\delta A_y^*}{\delta z} \right) \right\} \quad (3.80)$$

The values of  $A$ , and  $\delta A/\delta z$  can be calculated by convolving the Green's function along the source currents, as discussed in Section 3.4.2.

An aside observation is that if conductive materials are only placed in the region of  $x < 0$ , then heat flow is only in the direction of  $-\hat{z}$ . The total integral of  $P$  over the entire interface plane  $z = 0$  should give the total eddy current power loss within the material. This is one method to obtain the reflected resistance of the load to the terminals of the coil, i.e.

$$\Delta R = \frac{2}{I^2} \iint_{-\infty}^{+\infty} P(x, y) dx dy \quad (3.81)$$

where  $I$  is the current driven into the coil, and  $\Delta R$  is the terminal reflected resistance of the load, from the four-element model of Figure 2-2.

### 3.4.2 Implementation Details

To calculate the heating profile of an induction coil, the result shown in (3.80) can be applied by evaluating the  $\mathbf{A}$  field along the interface surface. First, to obtain the  $\mathbf{A}$  field at relevant points,  $N$  observational points are placed in a grid formation along the  $z = 0$  plane, and  $N$  points at a small distance above,  $z = \delta = 10^{-5}\text{m}$ . This results in  $2N$  observation points:  $\mathbf{O}_j = (O_{x,j}, O_{y,j}, O_{z,j}), j \in 1 \cdots 2N$ . The goal here is to convolve the dyadic Green's function over every filament, with each of the observational points fixed as the field points.

First, for a system of  $M$  filaments, we define the vector function  $\phi_j(\mathbf{r}), k \in 1 \cdots M$

with

$$\phi_j(\mathbf{r}) = \begin{cases} \hat{t}_j & \text{within the filament } j \\ 0 & \text{outside the filament } j \end{cases}$$

where  $\hat{t}_j$  is the unit vector tangential along the length of the filament. With this, the matrix  $\overline{\overline{L}}$  can be formed with each element at the  $j$ -th row and  $k$ -th column as

$$\overline{\overline{L}}_{jk} = \int_{S'} \overline{\overline{G}}(\mathbf{O}_j, \mathbf{r}') \cdot \phi_k(\mathbf{r}') dS' \quad (3.82)$$

Effectively, each entry of  $\overline{\overline{L}}$  is the Green's function, convolved over the support of the filament basis function  $\phi_k(\mathbf{r})$  for observational point  $\mathbf{O}_j$ . If the current of each filament  $I_j$  is combined into a column vector  $I$ , then the matrix equation can be written:

$$\overline{\overline{L}}I = A \quad (3.83)$$

Each row of  $A$  is the  $\mathbf{A}$  field measured at each of the  $2N$  observational points. To obtain a difference estimation of the gradient  $\delta\mathbf{A}/\delta z$ , take the difference between the first  $N$  field points measured at  $z = 0$  and the second  $N$  points measured at  $z = \delta$ , and divide the result by  $\delta$ . Substituting the evaluated  $A_x$ ,  $A_y$ ,  $\delta A_x/\delta z$  and  $\delta A_y/\delta z$  values for each observational point  $\mathbf{O}_j$  into (3.80), the value of the eddy current loss power flux is obtained at each observation point.

### 3.5 Comparison to Previous Analytical Models

Early seminal work in MQS partial differential equations have yielded a number of analytical solutions of the induction heating problem for the circular coil. In this section, we will compare the simulated predictions based on our method with existing analytical solutions.

The mutual impedance between two zero-volume circular filaments suspended above a semi-infinite half-plane can be written in the form of a Sommerfeld integral [58, 24, 19]:

$$Z_m = j\omega\mu_0\pi r_1 r_2 \int_0^\infty \left( e^{-k|d_1-d_2|} + \frac{k\mu_r - \eta}{k\mu_r + \eta} e^{-k(d_1+d_2)} \right) J_1(kr_1) J_1(kr_2) dk \quad (3.84)$$

with  $\eta^2 = k^2 + j\omega\mu_r\mu_0\sigma$ . The same solution can also be obtained by some minor algebra on the Dodds and Deeds solution [6], or by taking the associated Green's function from Section 3.2.1 and convolving it along the two circular contours in the

Hankel domain.

When solved for a circular coil, (3.84) gives the  $\Delta R$  and  $L_0 + \Delta L$  parts of the four-element model of Figure 2-2. The series resistance of the coil  $R_0$  must be separately evaluated.

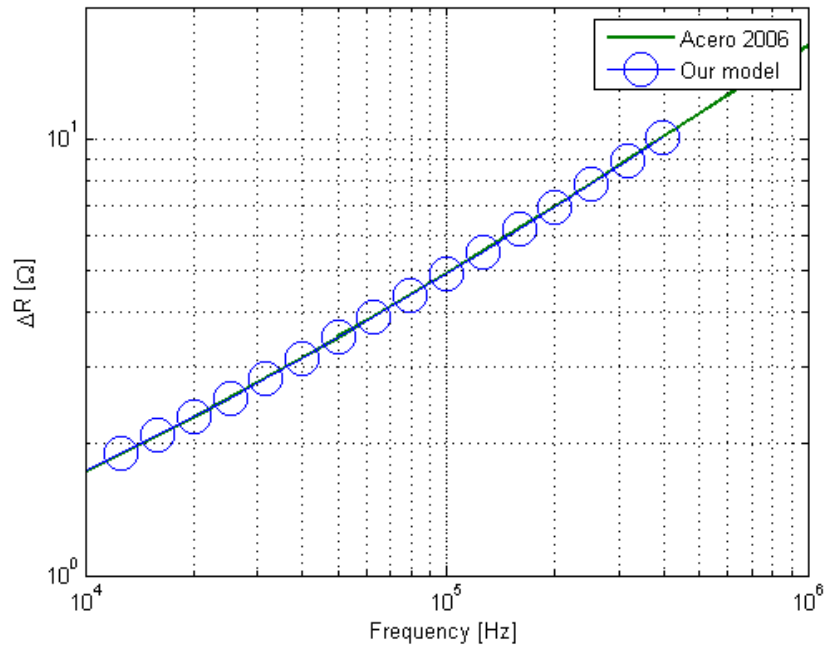
### 3.5.1 Acero et al.

Equation (3.84) was experimentally verified by Acero *et al.* for a 23-turn induction heating coil placed below a ferromagnetic plate [19]. We can recover the measurements made by Acero by evaluating (3.84) under the same conditions described. The heated ferromagnetic plate has the following properties:  $\mu_r = 130$ ,  $\sigma = 8 \times 10^6$  S/m. The plate is placed a distance of 4 mm above the coils. The coils are arranged as a series of flat concentric circular filaments, with 23 turns evenly spread from 2.5 cm to 10.5 cm. Evaluating the free-space mutual impedance Sommerfeld integral gives a frequency-independent free-space inductance of  $L_0 = 61.914 \mu\text{H}$ .

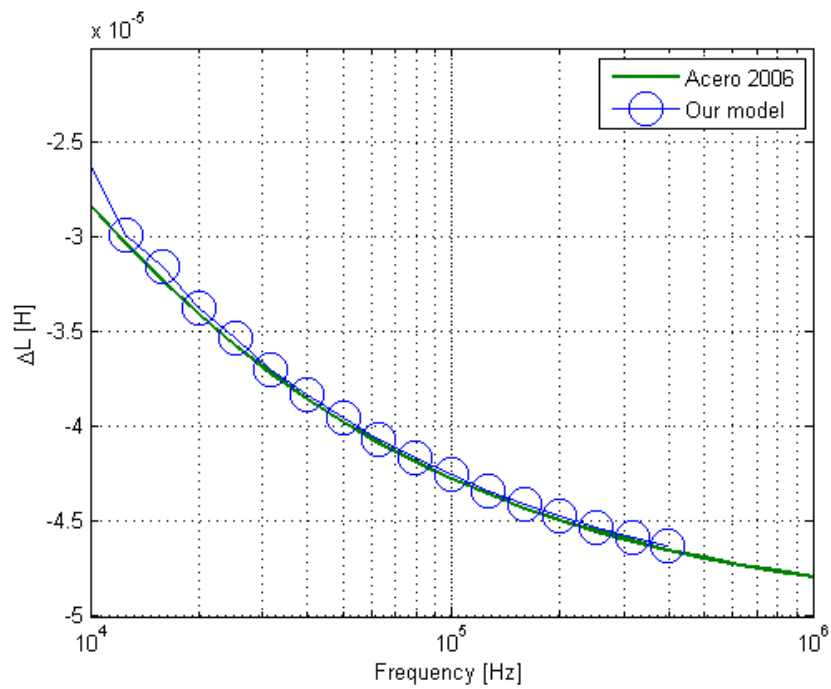
The Acero coil is then modeled using the three-dimensional filament method presented within this chapter as 23 concentric circles, with each circle discretized as 30 straight zero-volume filaments. The full Z matrix of these filaments are calculated with our technique, according to the steps described in Section 3.1. In Figure 3-3, the predictions of our model are compared to the experimental results from Acero *et al.* that were analytically recovered with (3.84), showing excellent agreement. Figure 3-4 shows the relative errors, defined here as the difference between our numerical results and the results measured by Acero, expressed as a fraction of Acero's results.

### 3.5.2 The effect of discretization

In order to study the effect of discretization, a single circular filament is discretized as 10, 15, 25, 63, 100 and 251 straight filaments respectively. For each discretization level, the  $\Delta R$  and  $\Delta L$  components of the terminal impedance are calculated and compared with that of the ideal solution from (3.84), shown in Figure 3-5. The relative errors of each discretization is evaluated and plotted in Figure 3-6. From these results it is clear that a discretization of around 25 filaments gives less than 2% relatively error, which is more than adequate for induction heating analysis when component tolerances and temperature variations are considered.



(a)



(b)

Figure 3-3: Comparison between the terminal impedance predicted by our three-dimensional filament model of a 23 turn coil system and those measured by Acero et al. [19] (a) Resistance; (b) Inductance.

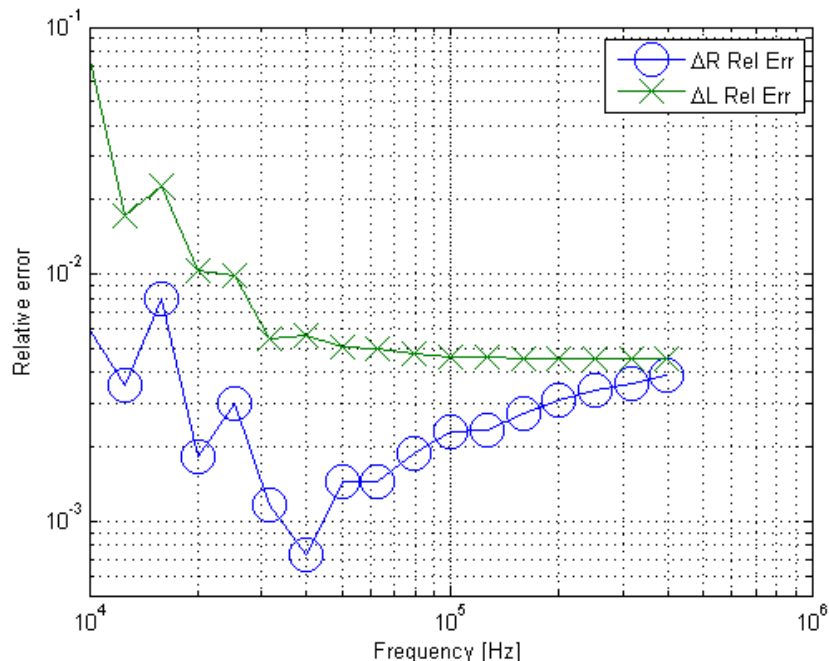


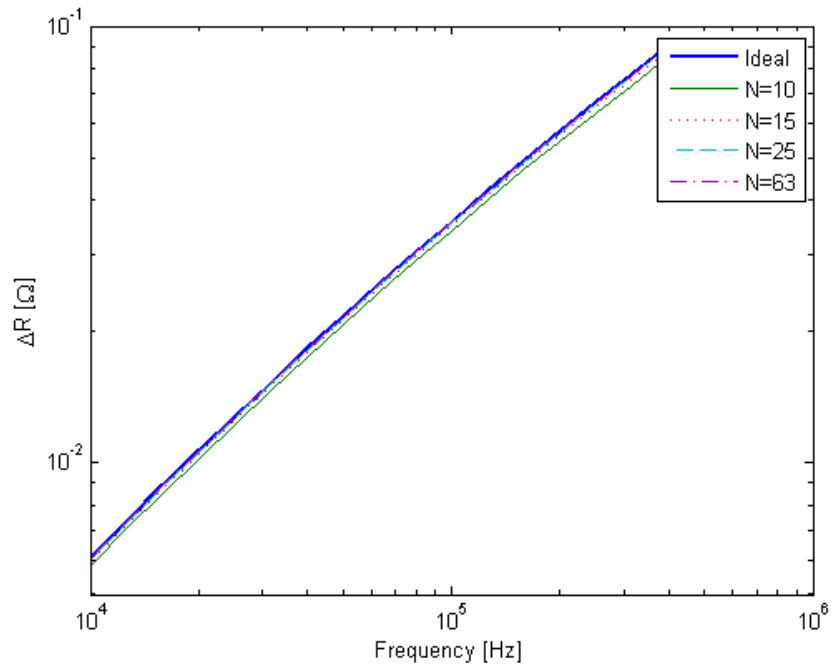
Figure 3-4: The relative errors of the terminal impedance predictions made by our three-dimensional filament model.

### 3.6 Experimental Validation

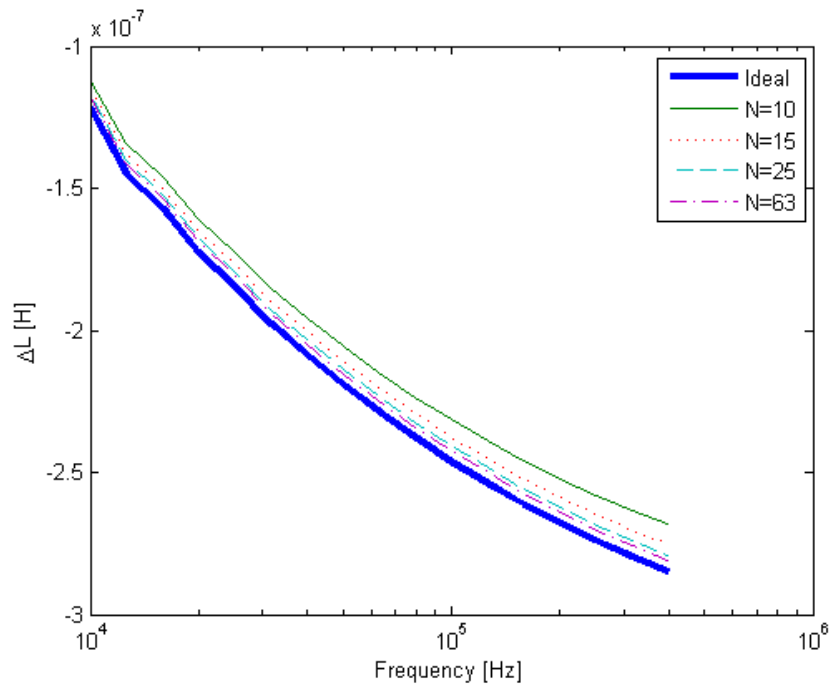
An additional experimental validation of the model was performed with a 31-turn flat spiral, wound with rectangular litz wires 1cm in cross-sectional height and approximately 2 mm in cross-sectional width. This coil is designed to heat a 9- or 10-inch pan, but the turns are distributed throughout the bottom of the pan to improve heat uniformity, according to the following pattern (see Figure 3-7):

- 8 turns between  $r=3.7$  cm and  $r = 4.8$  cm
- 10 turns between  $r = 6.65$  cm and  $r = 7.9$  cm
- 13 turns between  $r = 9.55$  cm and  $r = 11.2$  cm

The heated load used was a standard 9-inch cast iron skillet. The thickness of the pan was approximately 5 mm, greatly larger than the skin depth of cast iron even at 1 kHz of around 1 mm. For this reason, the pan can be accurately approximated as a semi-infinite surface in the model. The pan was spaced 2 mm above the top surface of the coil with cardboard, so that the center of the litz wire coil is approximately 7-8 mm below the heated surface.

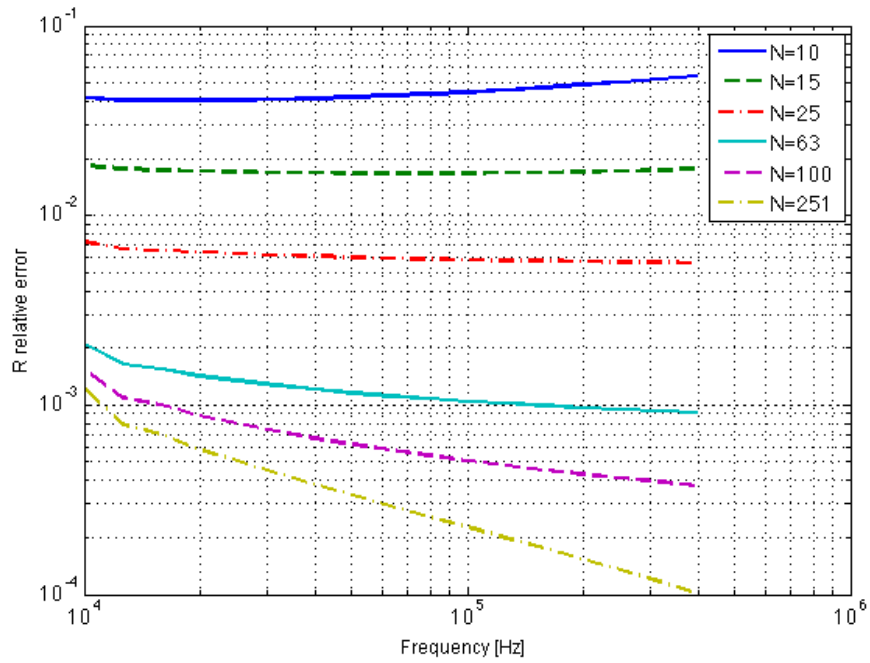


(a)

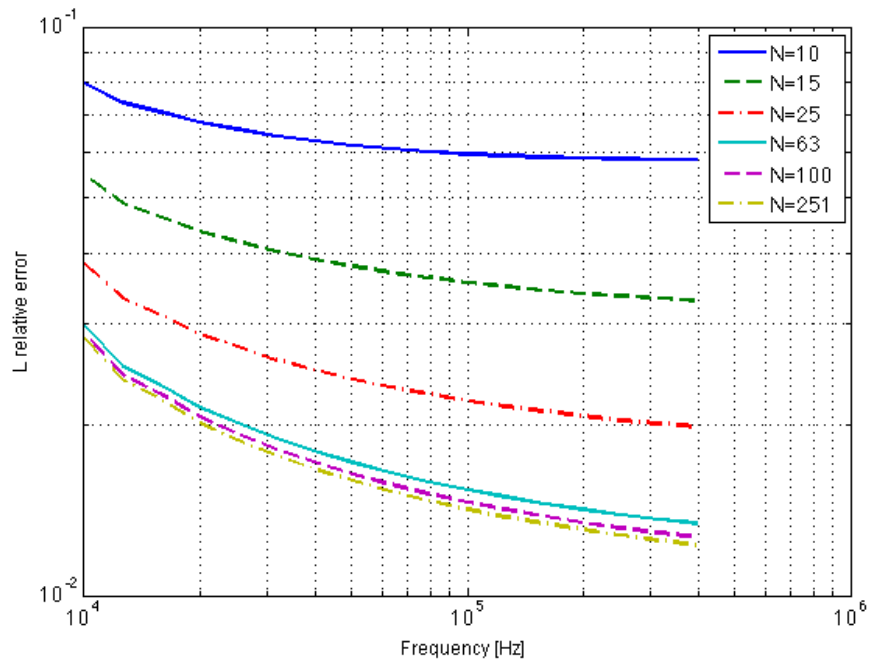


(b)

Figure 3-5: Comparison between the circular filament exact solution and results generated by piecewise linear discretization. (a) Terminal resistance  $\Delta R$ ; (b) Terminal inductance  $\Delta L$ .



(a)



(b)

Figure 3-6: Relative errors of the piecewise linear approximation of the circular filament. (a) Terminal resistance  $\Delta R$ ; (b) Terminal inductance  $\Delta L$ .

The frequency-dependent impedance of this experimental coil was measured with an LCR impedance analyzer and is shown in Figure 3-8. The results are parameterized using the four-element model of Figure 2-2. Here, the parameters  $\Delta R$  and  $\Delta L$  measure the contribution of the eddy currents in the pan to the electromagnetic fields generated by the coil.

To simulate the system described above, the contour of the spiral coil was modeled with 600 straight zero-volume filaments. The pan was modeled as a conductive, magnetic semi-infinite half-space, placed 10mm above the coil. The conductivity of the entire half-space was set to the bulk conductivity of cast iron, approximately  $\sigma = 1 \times 10^7$  S/m. However, it was considerably more difficult to select a single magnetic permeability value  $\mu_r$ , because it has a non-linear dependency with the strength of the magnetic field. Eventually, the value of  $\mu_r = 400$  was chosen by curve-fitting the simulated results to the measured values. This  $\mu_r$  lies within the reasonable range of values for cast iron exposed to very low magnetic field strengths (as is the case for the LCR impedance analyzer) and with some remanence left in the material. As shown in Figure 3-9, there is very good agreement between the measurements and the simulated results tuned with these parameters.

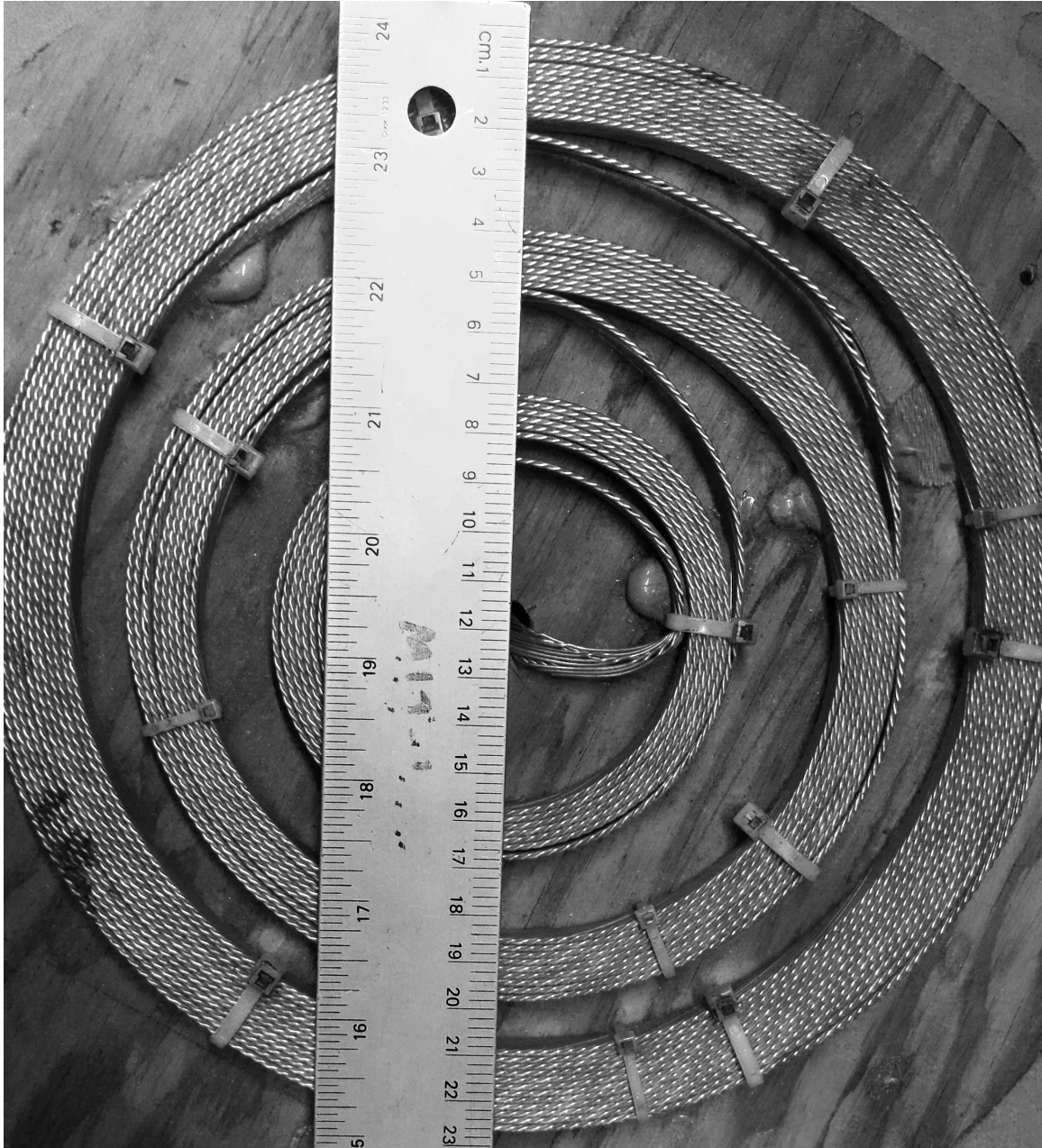
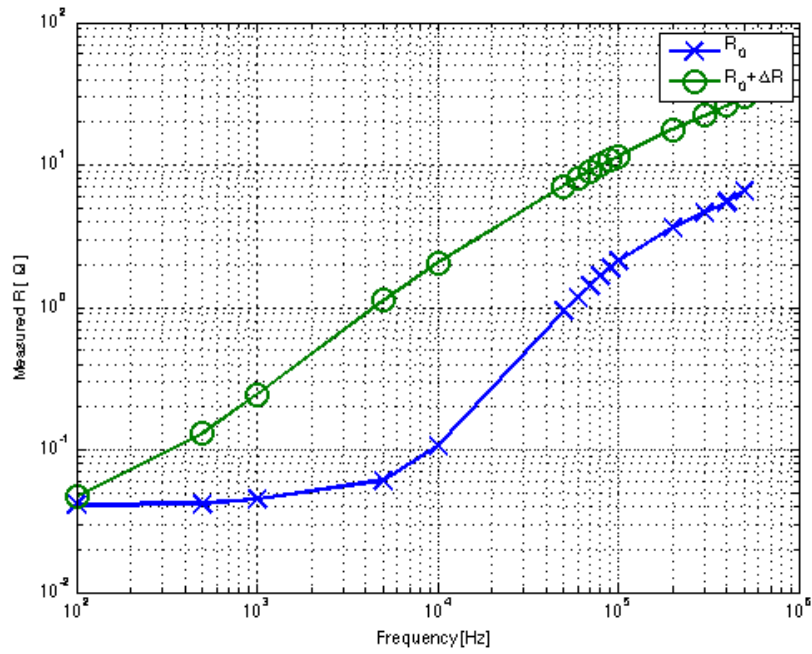
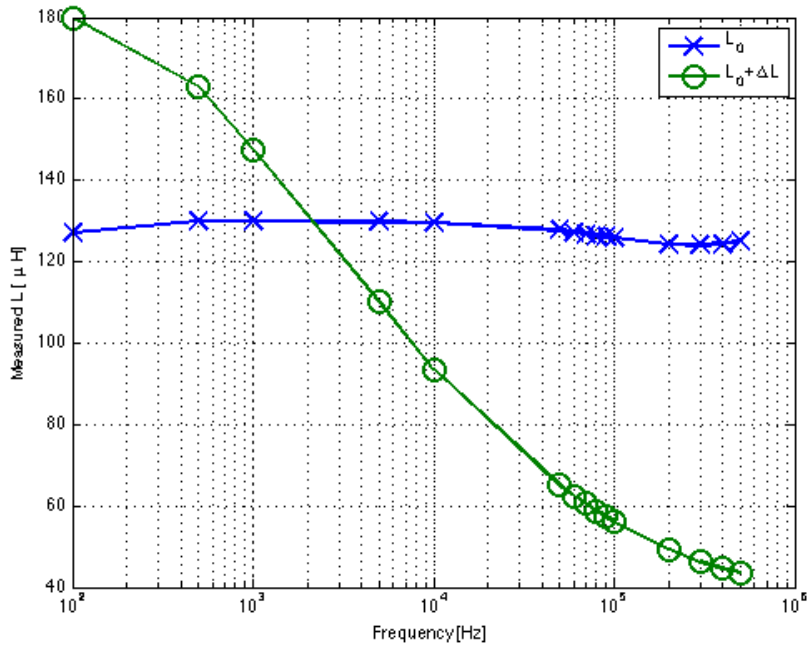


Figure 3-7: Dimensions of the measured litz wire coil

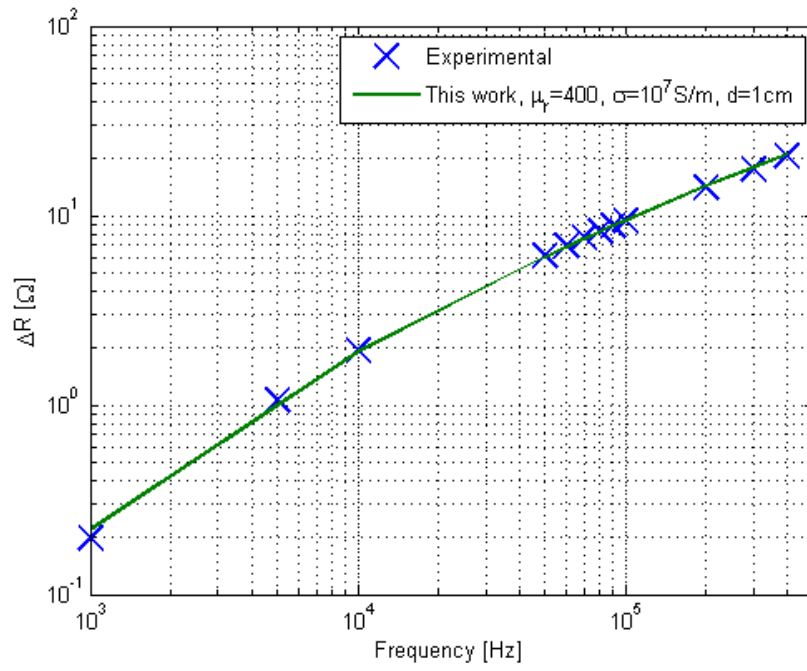


(a)

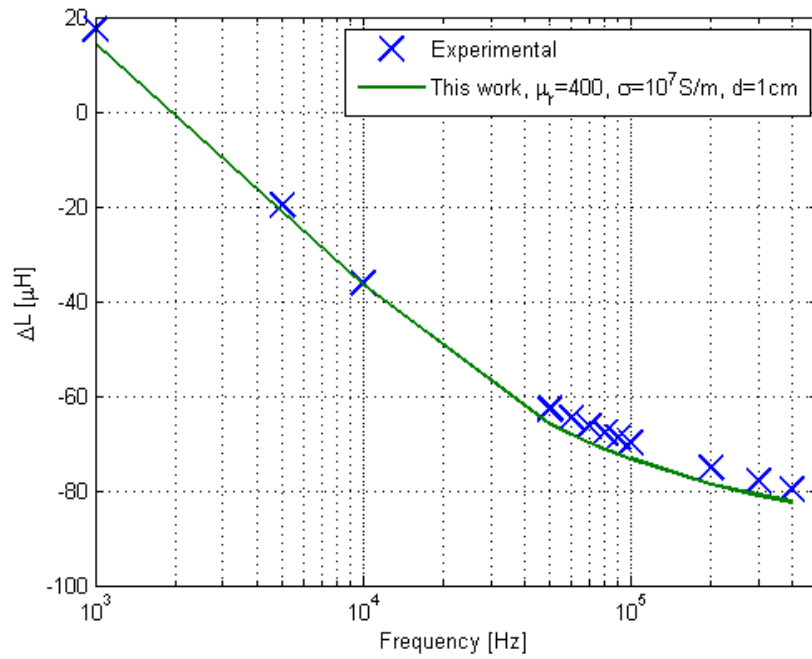


(b)

Figure 3-8: Measurements of the coil terminal impedance with and without the load: (a) resistances; (b) inductances.



(a)



(b)

Figure 3-9: Comparison of experimentally measured coil impedances with simulated results: (a) Resistances; (b) Inductances.

## 3.7 Performance

In this section, the computational speed of our technique is compared to that of existing tools widely used to design magnetic systems. The following benchmark tests were performed on a PC with an Intel Core 2 Duo 2.53 GHz Dual-Core CPU, 4 GB of RAM, running the 64-bit version of Windows 7.

Our PEEC model was implemented and executed in Matlab version 7.9.0 (R2009b), and utilized a three-dimensional interpolation algorithm for its look-up tables that was separately implemented in C++ and compiled into a Matlab executable or MEX file. We measured the evaluation speed for the mutual impedance between linear filaments at 7.915374 s for 1,000,000 filament pairs.

### Compared to FEM

The prevalent method for the analysis of induction heating system is by FEM. Here, we compared our method with the commercial FEM package COMSOL. In both cases, the 23 turn coil used by Acero *et al.* was modeled as a series of concentric coils, as previously described in Section 3.5.1.

In the first set of tests, the models were made with axial-symmetry explicitly enforced. In doing so, the order of both models is reduced from three dimensions ( $x, y, z$ ) to two ( $r, z$ ), dramatically reducing the size of the problem. Separate trials were conducted with the coil modeled both as zero-volume filaments and as finite-volume conductors. In the case of the FEM, the calculation domain was meshed to allow around 2% relative error in the calculated result. The average computation times over 10 trials are shown in Table 3.1. As shown here, our method is around 100 times faster the commercial FEM solver package for similar levels of accuracy.

Model	Conductor model	Time
FEM (COMSOL)	Filament	4.23 s
	Conductor	6.66 s
This work	Filament	0.039 s
	Conductor	0.060 s

Table 3.1: Speed benchmark of the axial-symmetric formulation.

In the second set of tests, the models were constructed as full three-dimensional models. It was no longer feasible to simulate the coil as finite-volume conductors within the FEM on our computer, due to the excessive memory requirements of the volumetric mesh. Instead, all trials were performed with zero-volume filaments. Two

FEM techniques were attempted here. In the first case, the full conductive domain representing the heated load was volumetrically meshed and the fields were solved for all domains. In the second case, the impedance boundary condition (IBC) [59] was used to avoid the meshing of the conductive domain, and the fields were solved only within the free-space. For all three methods, discretization and meshing were performed to control the relative error to around 2%. The average computation times over 3 trials are shown in Table 3.2. Once again, our method is around 100-200 times faster than the commercial FEM solver package for similar levels of accuracy.

Model	Conductor model	Time
FEM (COMSOL)	Filament	534 s
FEM with IBC (COMSOL)	Filament	252 s
This work	Filament	2.6 s

Table 3.2: Speed benchmark of the 3D Formulation

### Compared to other PEECs

It is helpful to get a sense of the speed achievable by comparing our method with the PEEC algorithm implemented by FastHenry. The two methods are very different in practice, as FastHenry cannot be used when magnetic materials are considered (i.e. when  $\mu_r \neq 1$ ). However in theory, the two methods differ only in how the Z matrix is calculated.

In the case of FastHenry, two calculation modes are available: a direct solve mode and a multipole expansion mode. In the direct solve mode, each element of the Z matrix is explicitly evaluated using closed-form solutions, such that the computational load of Z matrix is approximately  $\mathcal{O}[N^2]$ , where  $N$  is the number of filaments in the system. In the multipole mode, the filaments further away are fused together with the multipole expansion technique and solved together. After some initial overhead in preparation of the multipole matrices, the computational load is approximately  $\mathcal{O}[N]$ .

In comparison, our technique is strictly a direct solve approach. Due to the complex nature of the multilayered Green’s function, each element of the Z matrix must be explicitly calculated. For this reason, the computational load of our technique is also  $\mathcal{O}[N^2]$ . The multipole expansion cannot be used for order reduction because it is based on the  $1/r$  free-space Green’s function.

Table 3.3 shows the difference in speed between FastHenry and our technique for the formation of a  $1000 \times 1000$  Z matrix. As seen here, the direct solve speeds are

comparable between the two methods. However, the multipole expansion is able to reduce computation time by around 500, making FastHenry significantly faster than our technique. This computational advantage is a strong incentive for compression techniques (similar to the multipole expansion) to be adopted. The possible candidates include pre-corrected FFT [60], singular value decomposition [29] and partial reluctances [61].

Model	Time to evaluate 1,000,000 filament pairs
FastHenry (Direct Solve)	2.486 s
FastHenry (Multipole)	0.005 s
This work	7.9 s

Table 3.3: Comparison of mutual impedance computation speeds with established PEEC tools

## Chapter 4

# Optimal Design of an Induction Cooktop

The following chapter presents a design procedure for an induction cooking coil based upon mathematical single- and multiple-objective optimization algorithms. Similar approaches with optimization algorithms had been applied to the Transverse-Flux Heating (TFH) of metal strips [62, 36], the rapid heating of an injection mold plate [63], the design of a passive and active induction heating shield [33], and the design of an induction cooker [14]. In formulating their optimization strategies, these previous authors have placed heavy emphasis upon obtaining a uniform temperature profile in the heated load. For this reason, finite element method (FEM) models were used in many of these studies to capture the non-linear temperature- and field-dependent material effects. While highly accurate, FEM is unfortunately a very computationally expensive approach: each individual FEM evaluation can take from a few minutes to a few hours to complete. As a result, only relatively basic optimization techniques have been applied with relatively few degrees of freedom explored [4].

In the following chapter, the Partial Element Equivalent Circuit (PEEC) method developed in Chapter 3 is used in lieu of the FEM to evaluate and assess the performance of proposed coil designs. By reducing the run time from several minutes to less than 5 seconds for each coil evaluated, our PEEC method allows optimization to be performed with more advanced algorithms than those previously used for induction heating in the literature, and also over many more degrees of freedom than traditionally afforded. In particular, the simulated annealing algorithm [64] is used to find the global optimum for the single-objective problem, and the NSGA-II multi-objective genetic algorithm [65] is used to study the multiple-objective problem.

## 4.1 The Fitness Function

In computational design and optimization, the analyzed problem is typically posed as three distinct components:

1. An encoding / decoding algorithm that translates the vector of numbers representing points in the design space into physical designs understood by the software model.
2. A software model that simulates the physics of each design.
3. A scoring algorithm that analyzes the results of the software model and assigns fitness scores for the optimization algorithm to optimize.

Combined in series, these three components form what is known as the *fitness function*: a function that takes in a vector of numbers and outputs a set of fitness scores. The optimization algorithm is then tasked with the sole job of finding the vector of numbers that will minimize the fitness function.

### 4.1.1 Encoding Algorithm

Beyond simply summarizing the physical system into design degrees of freedom that can be vectorized and processed by a numerical optimization algorithm, the design of the encoding algorithm also shapes the fitness function within the design space. If the fitness function is shaped with fewer peaks and smoother, gentler gradients, then optimization algorithms will have an easier time traversing the design space and converging to the global optimum.

The approach used in this chapter is to constrain the coil to a spiral-path design, one that can be mathematically defined with the radius and height of the path as functions of the angle of rotation  $\theta$ . For a spiral of  $N$  turns, the encoding method defines the input vector  $x$  as

$$x = \begin{pmatrix} N \\ r_0 \\ z_0 \\ r_1 \\ z_1 \\ \vdots \\ r_m \\ z_m \end{pmatrix} \quad (4.1)$$

where  $r_0 \cdots r_m$ ,  $z_0 \cdots z_m$  are the radial and height functions  $r(\theta)$  and  $z(\theta)$ , sampled uniformly with respect to  $\theta$ . The starting points  $r_0$  and  $z_0$  are matched with  $r(\theta = 0)$  and  $z(\theta = 0)$  and the ending points  $r_m$  and  $z_m$  are matched with  $r(\theta = 2\pi N)$  and  $z(\theta = 2\pi N)$ . Additional turns can be added by incrementing the  $N$  parameter of the  $x$  vector. Defining the subscript  $k \in \mathbf{N} : 0 \leq k \leq m$ , one can write

$$r_k = r\left(k \cdot \frac{2\pi N}{m}\right), \quad z_k = z\left(k \cdot \frac{2\pi N}{m}\right) \quad (4.2)$$

The encoding algorithm then generates  $P$  linear piece-wise filaments to approximate the spiral, by uniformly resampling both  $r(\theta)$  and  $z(\theta)$  to  $P + 1$  points with cubic spline interpolation, and by generating linear filaments to connect these points together sequentially. This way, areas closer to the center of the spiral are modeled with shorter filaments than those further away, to ensure that parts of the coil with greater curvature gradients are more finely meshed.

Some additional modifications to this encoding scheme were added to improve the shape of the fitness function. Firstly, the sampled  $r_k$  values (but not  $z_k$ ) values are sorted to make the resultant radius function  $r(\theta)$  monotonically increasing with respect to  $\theta$ . Secondly, all values of  $x$  are normalized to lie within the range of 0 and 1 so that the bounded constraint can be readily applied to fix each coil parameter within sensible values.

### 4.1.2 The Electromagnetic Model

Given a set of conductive filaments, the PEEC model developed in Chapter 3 can be used to efficiently solve for the electromagnetic fields and heating fluxes within the system. Within the framework of the PEEC model, the coil system is modeled as the following:

- The  $z$  axis points in the upwards direction.
- Two semi-infinite half-spaces are defined with
  - free-space and the induction coil in the  $z > 0$  region,
  - the pan modeled as a custom-defined conductive magnetic material in the  $z < 0$  region and
  - the plane  $z = 0$  defined as the interface surface of interaction.
- The  $x$  and  $y$  axes are defined orthogonal to the  $z$  axis, on the surface of interaction.

- Linear filaments of arbitrary lengths and angles of rotation and inclination are generated, contained within the  $4 < z < 20$  mm and  $-20 < x, y < +20$  cm box region.

While fast and efficient, the PEEC model does make several approximations in pursuit of computational speed. The model requires everything to be linear by its inherent formulation, and so cannot accommodate properties that are field or temperature dependent. This effectively eliminates hysteresis as a loss mechanism. This is acceptable in the great majority of induction heating applications, because the heat effect due to hysteresis does not typically exceed 7% compared to the heat effect due to eddy current losses [66].

Another approximation made to enhance speed is to model the finite-volume conductors as zero-volume, point to point filaments. It was the empirical experience of the author and other works in literature such as [37] that optimization objectives within this thesis are not strongly affected by the cross-sectional area of the conductor itself. If necessary, the PEEC tool can also be used to simulate finite-volume conductors, although the computational cost of this is high and so was not pursued further.

### 4.1.3 Scoring Algorithm

The three major conflicting objectives for the design of the induction cooker coil are the cost of the coil, its efficiency and the resultant heat profile that it produces. After evaluating the fields for each coil design, the scoring algorithm should assign it three scores, one based on each of these three criteria. All the optimization algorithms used are minimizing algorithms (i.e. lower is better); where it is desired for a particular score to be maximized instead, the score can be inverted by multiplying with  $-1$ .

#### Cost

In a mass-production environment, the largest variable cost is the coil material itself. Holding the cross-sectional area of the wire used constant, a longer coil requires more copper to construct, and therefore will always cost more to manufacture. Here, the length of the coil is used as a proxy to rank the designs by their production costs.

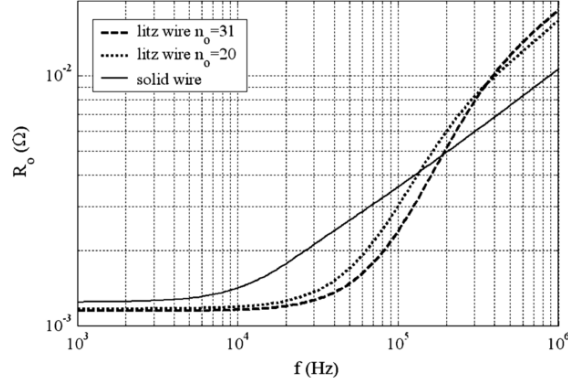


Figure 4-1: Series resistance for a loop of wire of different constructions: a 31-strand litz wire, AWG=24; a 20-strand litz wire, AWG=26; and a solid wire, AWG=11. [20]

## Efficiency

Referring to the equivalent circuit model of induction heating, the efficiency of the induction heating system can be written as

$$\eta_{ind} = \frac{R_D}{R_C + R_D} \quad (4.3)$$

where  $R_C$  is the resistance of the coil itself and  $R_D$  is the resistance of the plate. Here,  $R_C$  is relatively constant at low frequencies, driven by fixed geometrical parameters such as the conductor surface area and the length of the coil. However at higher frequencies, its value becomes frequency dependent due to the skin and proximity effects. The point where the dominance shifts and the resistance begins to increase is known as the knee frequency, and is an effect well-studied in literature. Figure 4-1 shows the knee frequency for some typical induction cooker coil materials (a solid wire and two versions of litz wires) to be between 20 kHz and 50 kHz.

Assuming that the frequency is sufficiently low, and that the coil material is suitably chosen to minimize the onset of the skin and proximity effects, (4.3) suggests that efforts to improve efficiency should be placed on maximizing the reflected resistance  $R_D$ . As explained in Chapter 1, this effect is strongly affected by the physical geometry of the coil relative to the conductive magnetic substrate. Assuming that the coil material is unchanged and that  $R_C$  per length of coil is fixed, the value of  $R_D$  per unit length becomes a good proxy metric to rank different designs on their efficiency.

An additional consideration is the fact that given two coils of equal efficiency, the

one with higher terminal resistance is more preferable, because it will require less current to power and thus less expensive IGBTs to drive in the power electronics stage. For the same  $R_D$  per unit length, a longer wire will cost more to manufacture, but will also reduce the costs of the power electronics. For this reason, the efficiency score was chosen to be the total value of  $R_D$  over the entire length of the coil.

## Temperature Profile

The steady-state heat equation has the form

$$k\nabla^2 T + \mathbf{q} = 0 \quad (4.4)$$

where  $T$  is the temperature,  $k$  is the thermal conductivity of the material and  $q$  is the heat source power density in  $W/m^2$ , which can be calculated at specified field points by the PEEC solver as explained in Chapter 3.

Assuming that the pan approximates a two-dimensional structure, a simple Finite Difference Method (FDM) model of the thermal system can be constructed by expanding the Laplacian in two dimensions. First, the bottom of the pan is overlaid with a uniform two-dimensional square grid, with the side of each cell having a length of  $\Delta x$ . Let the pan have a thickness of  $\Delta t$ , the thermal resistance between adjacent cells is:

$$R_{cond} = \frac{1}{k\Delta t} \quad (4.5)$$

The heat transfer coefficient  $h$  can be used to model the loss of heat due to convection and conduction to the ambient surroundings:

$$h = \frac{Q}{(T - T_{amb})(\Delta x)^2} \quad (4.6)$$

However, this equation is highly non-linear with temperature, and must be transformed or iteratively solved to obtain an accurate result. For optimization purposes however, speed is paramount, and instead the equation can be linearized around a specific temperature  $T_0 = 200^\circ\text{C}$ . The power loss to ambience is now  $Q_{amb} = Q_0 + R_{amb}\Delta T$ , where:

$$R_{amb} = \left[ \frac{dQ}{dT} \Big|_{T_0} \right]^{-1} = \frac{1}{(\Delta x)^2 \left[ h + \frac{dh}{dT} \right]_{T_0}} \quad (4.7)$$

$$Q_{amb} = (\Delta x)^2 (T - T_{amb}) h(T_0) \quad (4.8)$$

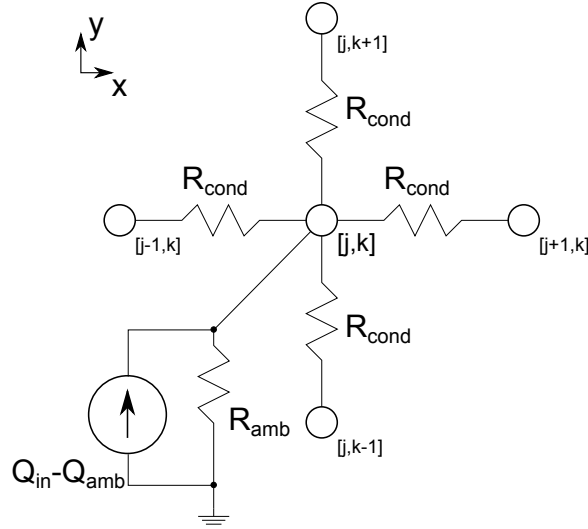


Figure 4-2: Finite difference method stencil of the thermal system, for the cell located at  $[j,k]$ .

$h$  is normally expressed as a function of the geometry of the system and the Rayleigh number of the convective fluid. Closed form solutions can be found in the literature, but the figures used here have been evaluated by using a commercial FEM solver.

Finally, the power input into each cell is set to be the power density at the center of the cell, multiplied by the area of the cell:

$$Q_{in} = (\Delta x)^2 q \quad (4.9)$$

The combined stencil of the thermal FDM model is shown in Figure 4-2. This system can then be solved to obtain a temperature profile over the surface of interaction at the bottom of the pan. The validity of these results are dependent on the assumptions: (1) the grid is sufficiently fine for the derivatives to be adequately approximated as differences; (2) the pan is thin enough to be approximated as a two-dimensional structure. With the temperature profile characterized, the score is taken to be the spread between the maximum and the minimum normalized temperature in the heated plate.

## 4.2 Single-Objective Optimization of Temperature Profile

It is clear that the single-objective optimization for cost and efficiency result in trivial solutions. In the case of cost, the solution is obvious: the lowest cost coil is to use

no coil at all; for high efficiency, the best coil is the one with as many large turns as possible, as close as possible to the heated surface.

By contrast, it is non-trivial to design an induction heating coil to achieve a uniform temperature profile. The single-objective optimization of the temperature profile is inherently non-linear, because it cannot be posed in a way for the objective function to be formulated as a linear combination of input variables, subject to linear constraints. In the following section, a two-part simulated annealing / hybrid pattern search algorithm is used to perform the single-objective optimization of the load temperature profile.

The optimization strategy used combines the ability of statistical methods to break away from local stationary points and converge towards global minimums, with the fast convergence speed of traditional algorithmic search techniques. In the first stage of the optimization, simulated annealing is chosen over genetic algorithms and other statistical methods for its mathematically sufficient ability to converge towards the global minimum given enough iterations<sup>1</sup>. The search is initiated with a 23-turn flat coil design from [19, 20, 11], shown in Figure 4-3. The radius of this initial coil is from 2.5 to 10.5 cm, and it is placed at a distance of 4mm from the load. The scheme uses Boltzmann Annealing to guarantee convergence towards the global optimum, and has 13 degrees of freedom: one that allows the number of turns to vary from 0 to 23, and the other twelve to define the radius function  $r(\theta)$  and the height function  $z(\theta)$ . The encoder generates 600 linear filaments, and the heat profile is evaluated for a  $30 \times 30$  square grid in the  $z = 0$  plane, spanning  $x, y = \pm 0.15$  m. Bicubically interpolating between these values, the temperature profile is calculated using the FDM scheme described above.

After 2500 iterations of simulated annealing, the normalized temperature spread drops from 11% in the initial design to 4%, which is an improvement of almost three. The resultant coil is shown in Figure 4-4. In the second stage of the optimization, a mixed general pattern search / Nelder-Mead simplex-method search is performed to converge upon the optimum point found by the simulated annealing algorithm. The search begins with the design found at the end of the simulated annealing algorithm. It then polls the design points around it according to pattern search rules and also according to the Nelder-Mead simplex-method rules [67]. If any of these polled points perform better than the original point, it is chosen as the newest best design, and the same process is repeated. Given that the step sizes are sufficiently small, the local

---

<sup>1</sup>An extensive discussion of the algorithm, the relevant terminology and its history can be found in [17].

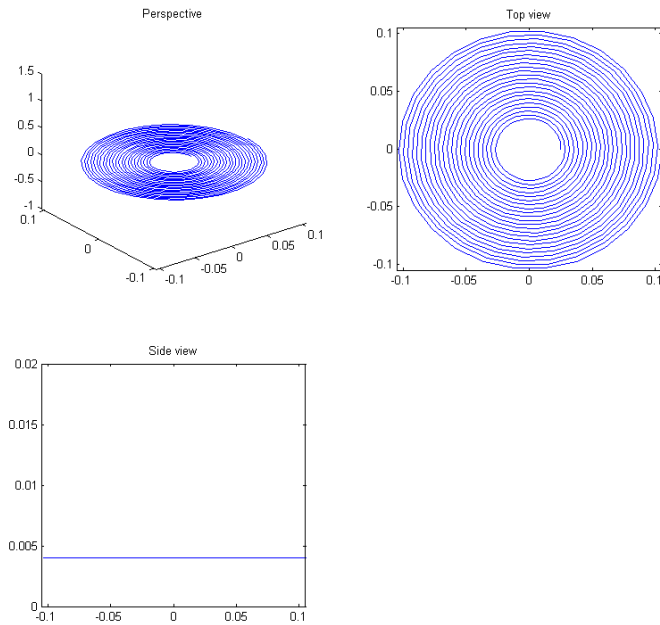


Figure 4-3: Original coil used as the starting point of the optimization analysis. Note that the pan is located *below* the coil at  $z = 0$ .

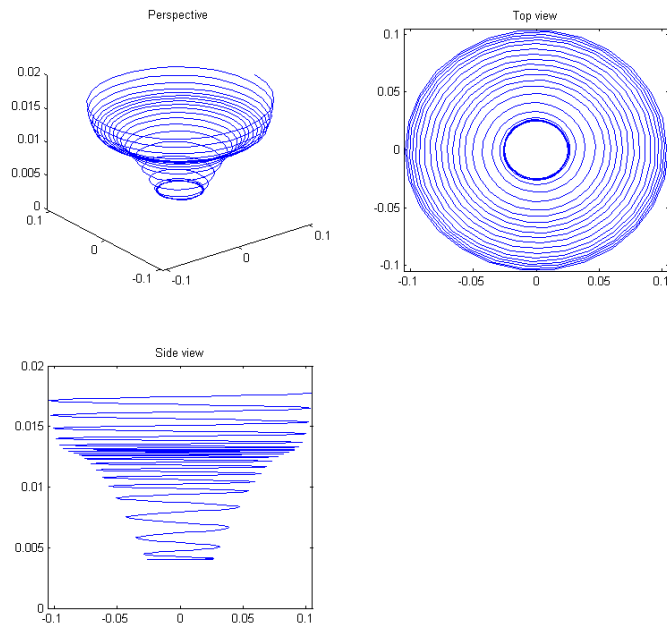


Figure 4-4: Improved coil after 2500 simulated annealing optimization iterations. Temperature spread score improves from 11% to 4%.

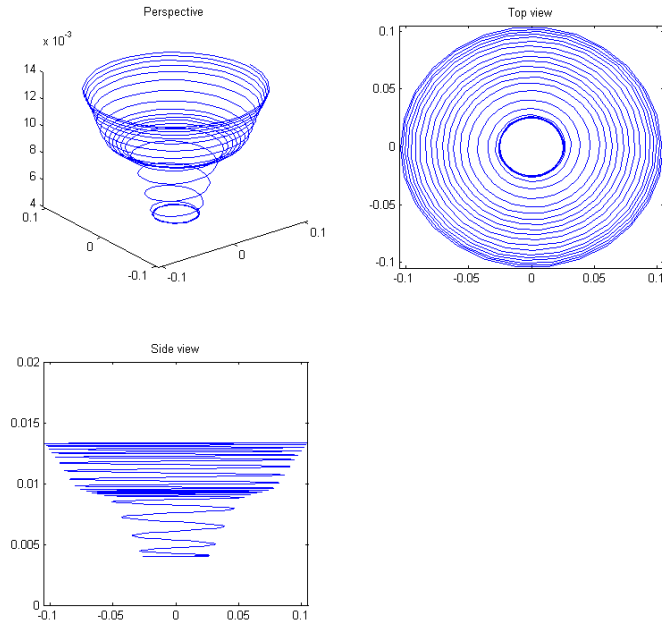


Figure 4-5: Improved coil at the end of the hybrid pattern search. Temperature spread is improved from 4% to 3.4%.

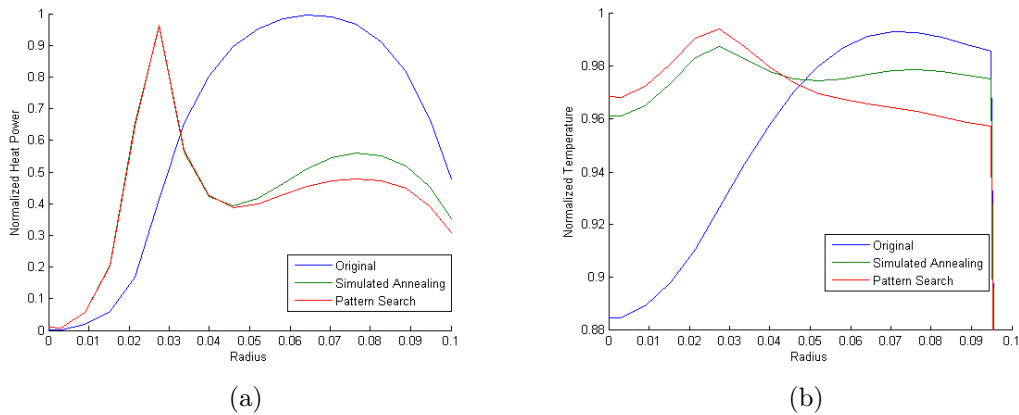
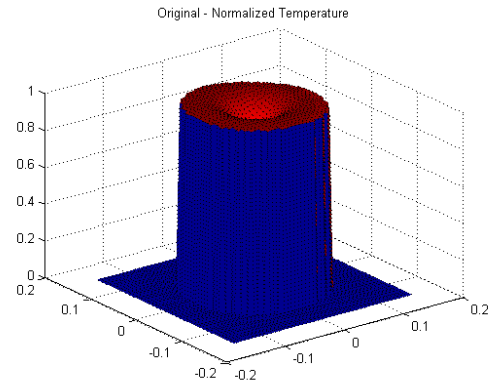
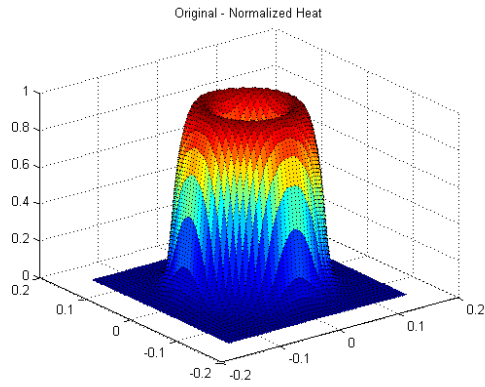
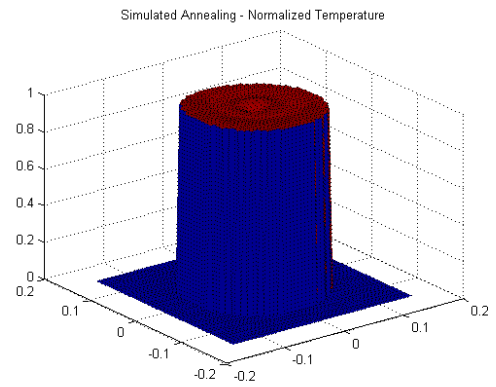
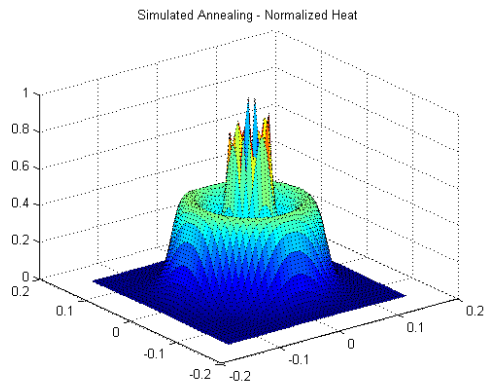


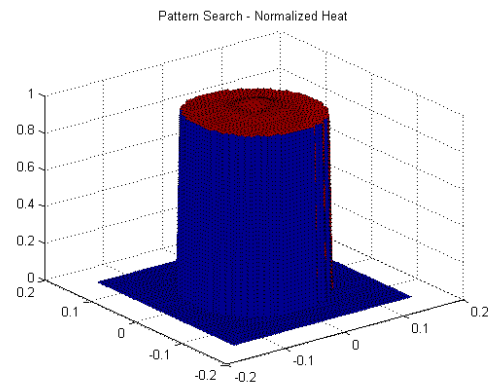
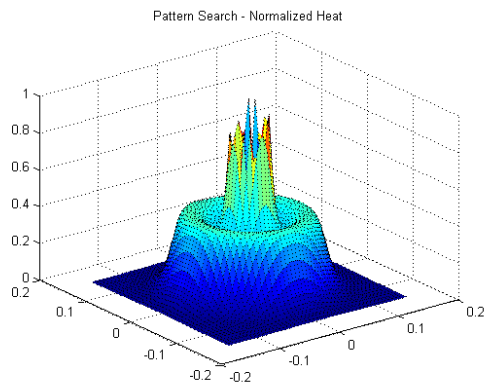
Figure 4-6: Comparison of the (a) heat and (b) temperature profiles of the three designs.



(a)



(b)



(c)

Figure 4-7: Heat and Temperature profiles of the three designs in 3D. (a) Original coil; (b) Coil optimized by simulated annealing; (c) Coil optimized by Hybrid pattern search.

region around the starting point is expected to be convex. If this is indeed the case, then the hybrid method is sufficient for convergence to the true optimum. After 65 iterations, the hybrid method improves the temperature spread further from 4% to 3.4%. The improved design is shown in Figure 4-5.

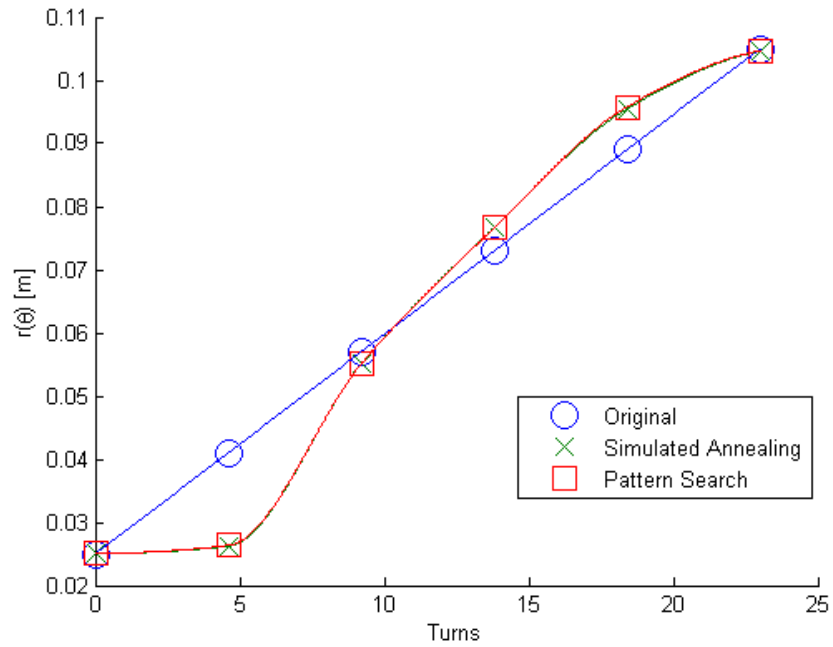
Figure 4-6 shows the heat and temperature profiles of the three designs as cross-sectional slices in the  $z$ - $r$  plane, starting from the center. Figure 4-7 shows these same results as three-dimensional surfaces. Seen here, a significant impediment to a uniform temperature profile is the coil's inability to heat the center of the load, an observation that agrees with other authors [14, 63]. The radius and height functions and their sampled values are plotted in Figure 4-8. As expected, the optimization algorithm has placed more turns of the coil towards the center and closer to the load in order to address the weaker heating ability there. However, an unexpected innovation found by the optimization algorithm is to place the outer turns further away from the load in the  $z$  direction.

### 4.3 Multi-Objective Optimization of Temperature, Efficiency and Cost

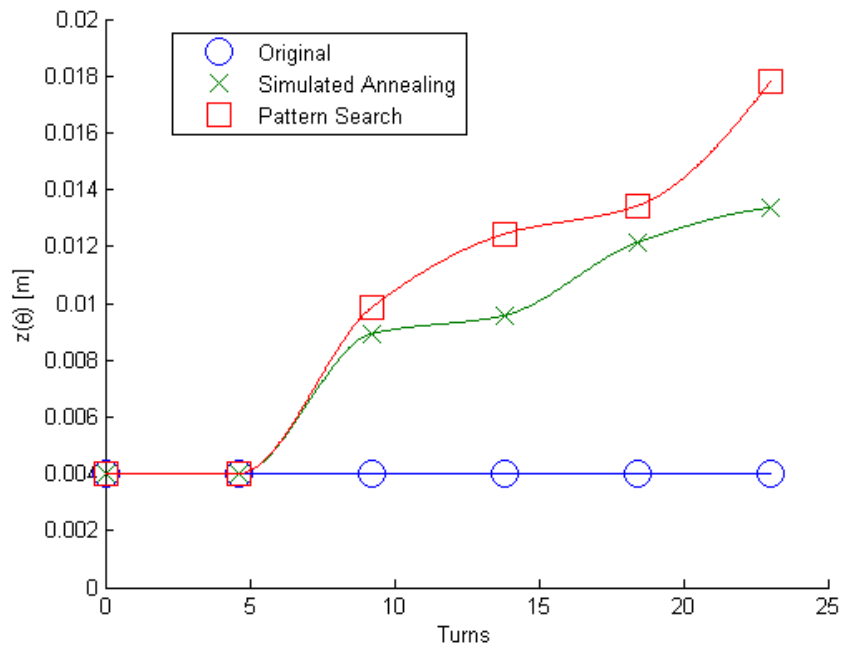
An optimization problem is said to be *multi-objective* when more than one cost or score function is considered. In this case, there is rarely an absolutely optimal solution, one that simultaneously out-performs all other solutions in all criteria. For example, there is no unique coil design that could simultaneously minimize cost, and maximize efficiency and temperature uniformity, due to the conflicting nature of these objectives. Instead, the goal is to discover a set of solutions at the trade-off boundaries between the different objectives, and to select one of these optimized solutions according to designer preferences. [68]

The solutions of multi-objective optimization are formally known as *Pareto optimal* solutions. A solution is considered to be Pareto optimal when it cannot be modified to improve its performance in one design objective without adversely affecting its performance in other objectives. By contrast, a non-Pareto optimal or a *dominated* solution is one that can be non-subjectively improved. For example a coil design that can be modified to be more efficient while still costing the same amount to manufacture is said to be dominated by the modified design, and is non-Pareto optimal.

A wide range of methods have been developed to solve the multi-objective opti-



(a)



(b)

Figure 4-8: Comparison of single-objective optimized coil designs. (a) Radiuses; (b) Heights.

mization problem, and review papers of the state-of-the art are available by Zitzler and Thiele [69], and by Marler and Arora [68]. Marler and Arora categorizes these methods into two distinct families:

- Traditional algorithms are based on collapsing the multi-objective cost functions down into a single cost function, and solving this new problem using an already established single-objective optimization algorithm. These techniques can be computationally efficient and easier to program, however their deterministic nature may prevent them from finding novel, globally optimal solutions.
- Genetic algorithms are stochastic methods based on the theory of natural selection. They act on populations of design, and solve for the multiple objectives directly. They are often complex to program, and may involve nuanced heuristics, but can produce more creative designs compared to traditional algorithms.

Multi-objective Genetic algorithms were used in this section to discover creative, unconventional coil designs that out-performs the traditional flat spiral coil. The algorithm used is the NSGA-II, developed by Deb *et al.* [65]. The algorithm uses elitism and a crowded operator that ranks the population based on both Pareto dominance and region density, with the aim of producing a set of Pareto optimal solutions spread apart over the Pareto frontier. The full NSGA-II approach was previously considered impractical for induction heating applications, due to the higher required population size and the high computation costs of FEM function evaluations [4]. It is made possible here by the high computational speed of the PEEC method.

The NSGA-II routine was executed for 117 generations of evolution, over 7081 function evaluations, lasting exactly 8 hours. The results are plotted as a three-dimensional Pareto frontier in Figure 4-9. Had the optimization been done using FEM at 1 minute per trial, we would expect at least 118 hours of computation to conduct 7081 function evaluations, which is approximately five continuous days. Three designs are selected from the multi-objective optimization (labeled 1-3 in Figure 4-9). Design 1 trades off about half of the  $\Delta R$  of the original design, but improves the heat profile by a factor of two, while also slightly reducing the cost of the coil. Design 2 matches the heat uniformity of the original coil, and decreases the length by a factor of two by reducing the  $\Delta R$  of the coil by around 75%. Design 3 performs approximately similar to the original coil, with a slightly worse heat profile and  $\Delta R$  but also slightly shorter length. The radius and height functions of the three new designs are plotted alongside the original prototype in Figure 4-10.

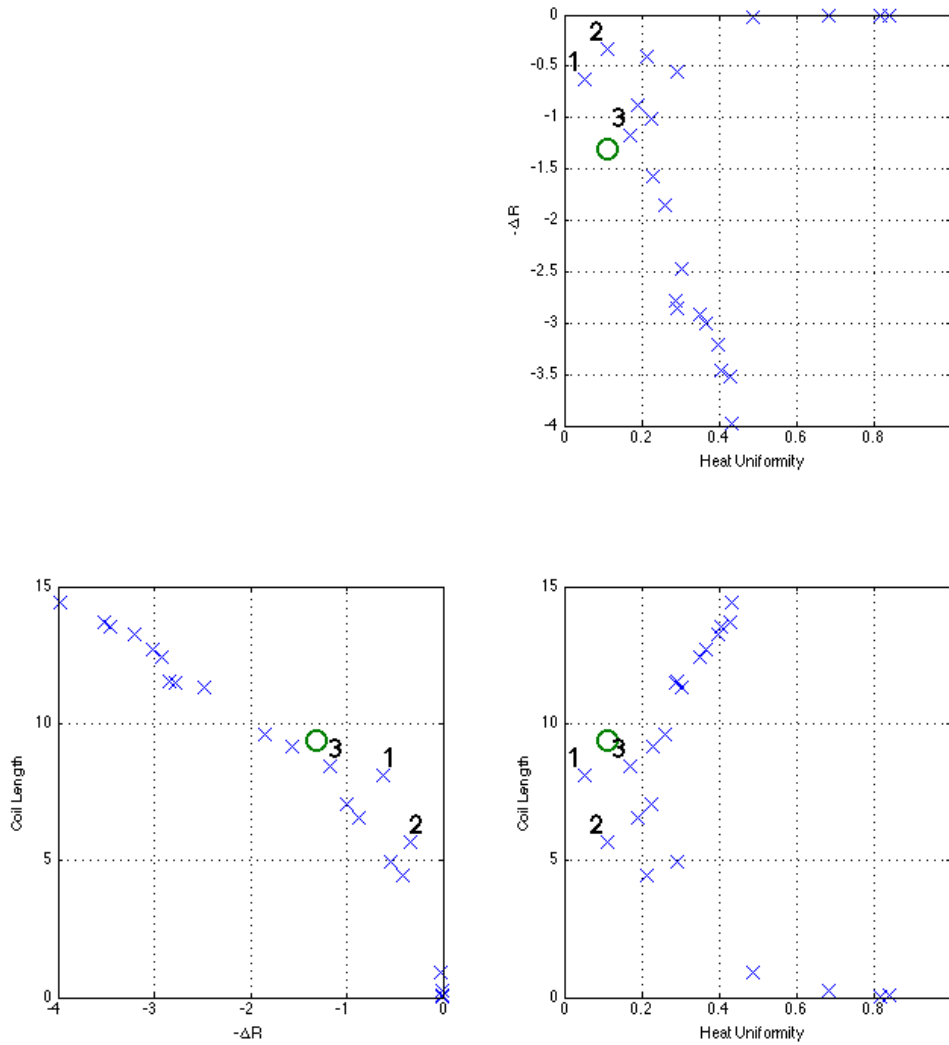
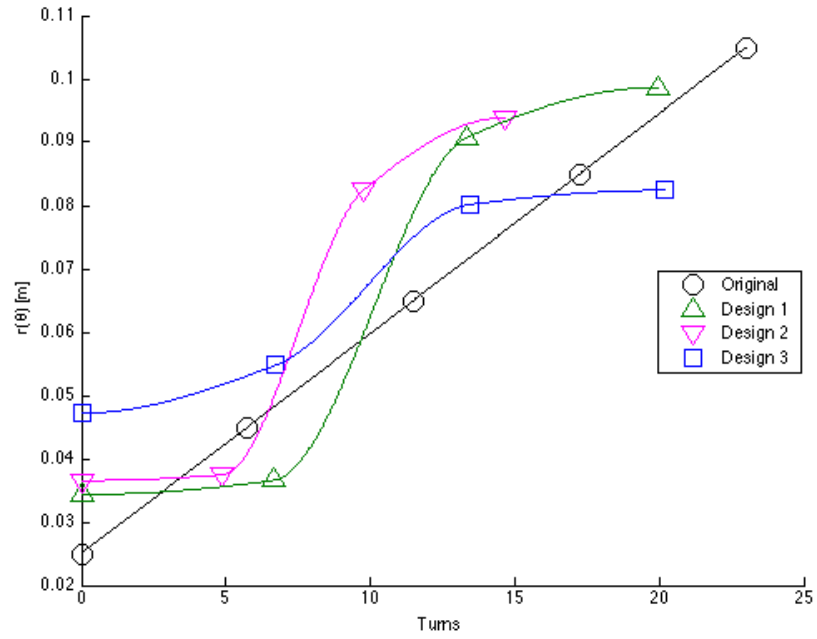
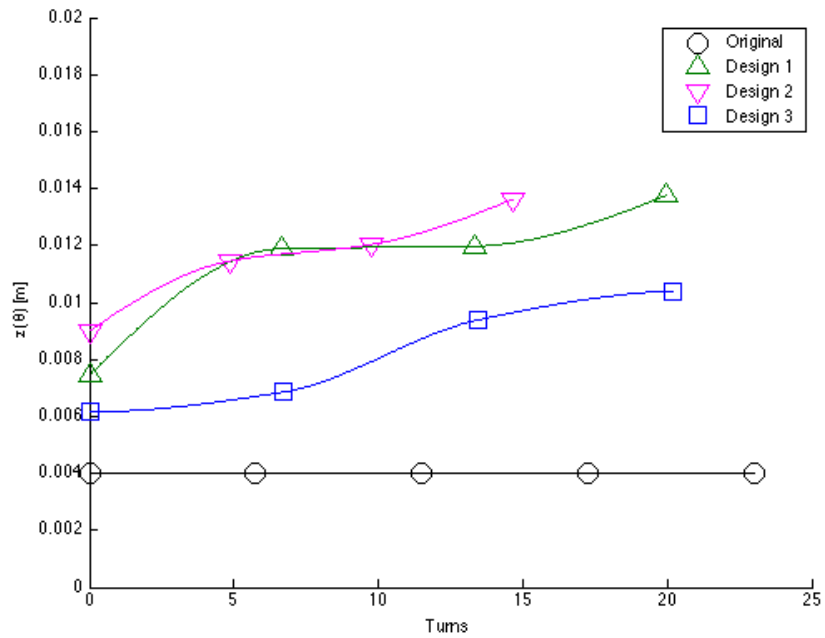


Figure 4-9: Results from multi-objective optimization with the NSGA-II Genetic Algorithm. The original prototype is shown as the dark green circle. The optimization algorithm is score-minimizing, and so lower scores (those closer to  $-\infty$ ) are better.



(a)



(b)

Figure 4-10: Comparison of multi-objective optimized coil designs. (a) Radiuses; (b) Heights.

# Chapter 5

## Conclusions and Future Work

In this thesis, it is shown that the multilayer Green’s function derived from the planar geometry of domestic induction heating can be used to substantially accelerate the computation of magnetoquasistatic electromagnetic fields. Controlling for similar levels of relative error, our PEEC solver was able to perform at speeds of 100+ times faster than the tested commercial FEM package, an improvement of two orders of magnitude.

Our PEEC solver was used to perform the single-objective optimization of the load temperature profile, as well as the multi-objective optimization of the temperature, efficiency and cost. In both cases, the optimization algorithms used—Simulated Annealing and NSGA-II—were previously deemed impractical due to the high computational costs of fitness function evaluations. Both optimization algorithms produced novel, three-dimensional induction coil designs.

Further improvements to the results of this thesis can be made in the following two areas:

**Compression techniques.** The bottleneck of the PEEC method proposed within this thesis is the formation of the dense  $Z$  matrix, currently formed at complexity order  $\mathcal{O}[N^2]$ . Significant speed advantages can be gained by compression / sparsification techniques, such as pre-corrected Fourier transform [60, 70], singular value decomposition [29] and partial reluctances [61]. It was shown in Section 3.7 that the use of the Fast Multipole Method compression technique reduced the complexity of FastHenry to approximately  $\mathcal{O}[N]$ , and increased its speed by two to three orders of magnitude.

**More comprehensive optimization routines.** The optimization routine within this thesis retained the spiral property of the induction coil, and applied “vanilla” versions of two popular optimization algorithms. The “no free lunch” theorem of op-

timization asserts that no universal optimization algorithm exists that is efficient for all classes of problems [71], and this suggests that further gains can be obtained if the algorithms are adapted for their specific applications. Indeed, customized versions of both algorithms are widespread for the induction heating application [4]. Improvements on the optimization algorithms could allow more degrees of freedom to be explored in the design of the coil with fewer function evaluations.

# Bibliography

- [1] J. Acero, J. Burdio, L. Barragan, D. Navarro, R. Alonso, J. Garcia, F. Monterde, P. Hernandez, S. Llorente, and I. Garde, “Domestic Induction Appliances,” *IEEE Industry Applications Magazine*, vol. 16, no. 2, pp. 39–47, 2010.
- [2] A. Fujita, H. Sadakata, I. Hirota, H. Omori, and M. Nakaoka, “Latest Developments of High-Frequency Series Load Resonant Inverter Type Built-In Cooktops for Induction Heated All Metallic Appliances,” in *IEEE IPERC '09*, vol. 3, 2009, pp. 2537–2544.
- [3] L. Chambers, Ed., *The Practical Handbook of Genetic Algorithms: Applications, Second Edition*. Chapman and Hall/CRC, 2000.
- [4] C. Coello and G. Lamont, Eds., *Applications Of Multi-Objective Evolutionary Algorithms (Advances in Natural Computation)*. World Scientific Pub Co Inc, 2004.
- [5] H. Koertzen, J. van Wyk, and J. Ferreira, “Design of the half-bridge, series resonant converter for induction cooking,” in *Power Electronics Specialists Conference, 1995. PESC'95 Record., 26th Annual IEEE*, vol. 2. IEEE, 1995, pp. 729–735.
- [6] C. Dodd, “Analytical Solutions to Eddy-Current Probe-Coil Problems,” *Journal of Applied Physics*, vol. 39, no. 6, pp. 2829–2838, 1968.
- [7] M. Adler, “A field-theoretical approach to magnetic induction heating of thin circular plates,” *IEEE Transactions on Magnetics*, vol. 10, no. 4, pp. 1118–1125, Dec. 1974.
- [8] W. Hurley and J. Kassakian, “Induction heating of circular ferromagnetic plates,” *IEEE Transactions on Magnetics*, vol. 15, no. 4, pp. 1174–1181, Jul. 1979.
- [9] W. Roshen and D. Turcotte, “Planar inductors on magnetic substrates,” *IEEE Transactions on Magnetics*, vol. 24, no. 6, pp. 3213–3216, 1988.
- [10] W. Roshen, “Effect of finite thickness of magnetic substrate on planar inductors,” *IEEE Transactions on Magnetics*, vol. 26, no. 1, pp. 270–275, 1990.

- [11] J. Acero, R. Alonso, L. Barragán, and J. Burdio, “Modeling of planar spiral inductors between two multilayer media for induction heating applications,” *Magnetics, IEEE Transactions on*, vol. 42, no. 11, pp. 3719–3729, 2006.
- [12] J. Acero, R. Alonso, J. M. Burdio, L. a. Barragan, and S. Llorente, “Electromagnetic induction of planar windings with cylindrical symmetry between two half-spaces,” *Journal of Applied Physics*, vol. 103, no. 10, p. 104905, 2008.
- [13] H. Koertzen, J. van Wyk, and J. Ferreira, “Investigating the influence of material properties on the efficiency of an induction heating load transformer using FEM simulations,” in *IAS '95. Conference Record of the 1995 IEEE Industry Applications Conference Thirtieth IAS Annual Meeting*, vol. 1. IEEE, 1995, pp. 868–873.
- [14] J.-k. Byun, K. Choi, H. Roh, and S.-y. Hahn, “Optimal design procedure for a practical induction heating cooker,” *Magnetics, IEEE Transactions on*, vol. 36, no. 4, pp. 1390–1393, 2000.
- [15] J. Lavers, “State of the art of numerical modeling for induction processes,” *COMPEL: The International Journal for Computation and Mathematics in Electrical and Electronic Engineering*, vol. 27, no. 2, pp. 335–349, 2008.
- [16] A. E. Ruehli, “Inductance Calculations in a Complex Integrated Circuit Environment,” *IBM Journal of Research and Development*, vol. 16, no. 5, pp. 470–481, Sep. 1972.
- [17] L. Ingber, “Adaptive simulated annealing (ASA): Lessons learned,” *Control and Cybernetics*, 1996.
- [18] A. Mühlbauer, “History of induction heating and melting,” 2008.
- [19] J. Acero, R. Alonso, J. Burdio, L. Barragán, and D. Puyal, “Analytical equivalent impedance for a planar circular induction heating system,” *Magnetics, IEEE Transactions on*, vol. 42, no. 1, pp. 84–86, 2006.
- [20] —, “Frequency-dependent resistance in litz-wire planar windings for domestic induction heating appliances,” *Power Electronics, IEEE Transactions on*, vol. 21, no. 4, pp. 856–866, 2006.
- [21] H. A. Haus and J. R. Melcher, *Electromagnetic fields and energy*. Prentice-Hall, 1989.
- [22] J. Ferreira, “Analytical computation of AC resistance of round and rectangular litz wire windings,” *Electric Power Applications, IEE Proceedings B*, vol. 139, no. 1, pp. 21–25, 1992.

- [23] C. Sullivan, "Optimal choice for number of strands in a litz-wire transformer winding," in *PESC97. Record 28th Annual IEEE Power Electronics Specialists Conference. Formerly Power Conditioning Specialists Conference 1970-71. Power Processing and Electronic Specialists Conference 1972*, vol. 1. IEEE, 1997, pp. 28–35.
- [24] W. Hurley and M. Duffy, "Calculation of self and mutual impedances in planar magnetic structures," *IEEE Transactions on Magnetics*, vol. 31, no. 4, pp. 2416–2422, Jul. 1995.
- [25] —, "Calculation of self-and mutual impedances in planar sandwich inductors," *Magnetics, IEEE Transactions on*, vol. 33, no. 3, pp. 2282–2290, 1997.
- [26] S. Hui and W. Ho, "A new generation of universal contactless battery charging platform for portable consumer electronic equipment," *Power Electronics, IEEE Transactions on*, vol. 20, no. 3, pp. 620–627, 2005.
- [27] W. Tang, *Transforming Domain into Boundary Integrals in Bem: A Generalized Approach (Lecture Notes in Engineering)*. Springer-Verlag, 1988.
- [28] M. Kamon, M. Ttsuk, and J. White, "FASTHENRY: a multipole-accelerated 3-D inductance extraction program," *IEEE Transactions on Microwave Theory and Techniques*, vol. 42, no. 9, pp. 1750–1758, 1994.
- [29] W. Kao, C. Lo, and M. Basel, "Parasitic extraction: Current state of the art and future trends," *Proceedings of the IEEE*, vol. 89, no. 5, pp. 729–739, 2001.
- [30] E. Rosa, "The self and mutual inductances of linear conductors," 1908.
- [31] F. W. Grover, *Inductance Calculations: Working Formulas and Tables*, second edi ed. New York: Dover, 1962.
- [32] C. Hoer and C. Love, "Exact inductance equations for rectangular conductors with applications to more complicated geometries," *Journal of Research of the National Bureau of Standards – C. Engineering and Instrumentation*, vol. 69C, no. 2, pp. 127–137, 1965.
- [33] P. Sergeant, L. Dupre, M. De Wulf, and J. Melkebeek, "Optimizing active and passive magnetic shields in induction heating by a genetic algorithm," *IEEE Transactions on Magnetics*, vol. 39, no. 6, pp. 3486–3496, Nov. 2003.
- [34] A. Niknejad and R. Meyer, "Analysis, design, and optimization of spiral inductors and transformers for Si RF ICs," *IEEE Journal of Solid-State Circuits*, vol. 33, no. 10, pp. 1470–1481, 1998.
- [35] D. Sitaram, Y. Zheng, and K. Shepard, "Full-chip, three-dimensional, shapes-based RLC extraction," *IEEE Transactions on Computer-Aided Design of Integrated Circuits and Systems*, vol. 23, no. 5, p. 711, 2004.

- [36] P. Alotto, A. Spagnolo, and B. Paya, “Particle Swarm Optimization of a Multi-Coil Transverse Flux Induction Heating System,” *IEEE Transactions on Magnetics*, vol. 47, no. 5, pp. 1270–1273, May 2011.
- [37] A. Niknejad and R. Meyer, “Analysis of eddy-current losses over conductive substrates with applications to monolithic inductors and transformers,” *IEEE Transactions on Microwave Theory and Techniques*, vol. 49, no. 1, pp. 166–176, 2001.
- [38] R. Ditchburn and S. Burke, “Planar rectangular spiral coils in eddy-current non-destructive inspection,” *NDT & E International*, vol. 38, no. 8, pp. 690–700, Dec. 2005.
- [39] J. Shen, *Computational Electromagnetics Using Boundary Elements: Advances in Modelling Eddy Currents (Topics in Engineering)*. Computational Mechanics, 1995.
- [40] R. Sabariego, P. Sergeant, J. Gyselinck, P. Dular, L. Dupre, and J. Melkebeek, “Fast multipole accelerated finite element-boundary element analysis of shielded induction heaters,” *IEEE Transactions on Magnetics*, vol. 42, no. 4, pp. 1407–1410, Apr. 2006.
- [41] T. Todaka and M. Enokizono, “Optimal design method with the boundary element for high-frequency quenching coil,” *IEEE Transactions on Magnetics*, vol. 32, no. 3, pp. 1262–1265, May 1996.
- [42] P. Sergeant, U. Adriano, L. Dupre, O. Bottauscio, M. DeWulf, M. Zucca, and J. Melkebeek, “Passive and Active Electromagnetic Shielding of Induction Heaters,” *IEEE Transactions on Magnetics*, vol. 40, no. 2, pp. 675–678, Mar. 2004.
- [43] J. Juillard and B. D. Barmon, “Simple analytical three-dimensional eddy-current model,” *IEEE Transactions on Magnetics*, vol. 36, no. 1, pp. 258–266, 2000.
- [44] J. Bowler, “Eddy current calculations using half-space Green’s functions,” *Journal of applied physics*, 1987.
- [45] J. Acero, R. Alonso, J. Burdio, and L. Barragan, “Enhancement of induction heating performance by sandwiched planar windings,” *Electronics Letters*, vol. 42, no. 4, p. 241, 2006.
- [46] A. E. Siegman, “Quasi fast Hankel transform,” *Optics Letters*, vol. 1, no. 1, p. 13, Jul. 1977.
- [47] M. Guizar-Sicairos and J. C. Gutierrez-Vega, “Computation of quasi-discrete Hankel transforms of integer order for propagating optical wave fields,” *Journal of the Optical Society of America A*, vol. 21, no. 1, p. 53, Jan. 2004.

- [48] V. Magni, G. Cerullo, and S. De Silvestri, “High-accuracy fast Hankel transform for optical beam propagation,” *Journal of the Optical Society of America A*, vol. 9, no. 11, p. 2031, Nov. 1992.
- [49] T. M. Pritchett, “Fast Hankel Transform Algorithms for Optical Beam Propagation,” Army Research Laboratory, Tech. Rep. December, 2001.
- [50] L. Yu, M. Huang, M. Chen, and W. Chen, “Quasi-discrete Hankel transform,” *Optics letters*, 1998.
- [51] T. Gerstner and M. Griebel, “Numerical integration using sparse grids,” *Numerical algorithms*, 1998.
- [52] I. Sloan and S. Joe, *Lattice methods for multiple integration*. Oxford: Clarendon Press, 1994.
- [53] J. Gentle, “Random number generation and Monte Carlo methods,” 2003.
- [54] P. van Dooren and L. de Ridder, “An adaptive algorithm for numerical integration over an N-dimensional cube,” *Journal of Computational and Applied*, 1976.
- [55] A. Genz and A. Malik, “Remarks on algorithm 006: An adaptive algorithm for numerical integration over an N-dimensional rectangular region,” *Journal of Computational and Applied Mathematics*, 1980.
- [56] F. Heiss and V. Winschel, “Likelihood approximation by numerical integration on sparse grids,” *Journal of Econometrics*, vol. 144, no. 1, pp. 62–80, May 2008.
- [57] H. Greenhouse, “Design of planar rectangular microelectronic inductors,” *Parts, Hybrids, and Packaging, IEEE Transactions on*, vol. 10, no. 2, pp. 101–109, 1974.
- [58] J. A. Tegopoulos and E. Kriezis, *Eddy Currents in Linear Conducting Media (Studies in Electrical and Electronic Engineering)*. Elsevier Science Ltd, 1984.
- [59] T. B. A. Senior, “Impedance boundary conditions for imperfectly conducting surfaces,” *Applied Scientific Research, Section B*, vol. 8, no. 1, pp. 418–436, Dec. 1960.
- [60] J. White, J. Phillips, and T. Korsmeyer, “Comparing Precorrected-FFT and Fast Multipole Algorithms for Solving Three-Dimensional Potential Integral Equations,” in *Proceedings of the Colorado Conference on Iterative Methods, Breckenridge, Colorado*. Citeseer, 1994.
- [61] A. Devgan, H. Ji, and W. Dai, “How to efficiently capture on-chip inductance effects: introducing a new circuit element K,” in *Proceedings of the 2000 IEEE/ACM international conference on Computer-aided design*. IEEE Press, 2000, pp. 150–155.

- [62] P. Di Barba, F. Dughiero, and A. Savini, “Multiobjective shape design of an inductor for transverse-flux heating of metal strips,” *IEEE Transactions on Magnetics*, vol. 39, no. 3, pp. 1519–1522, May 2003.
- [63] M.-S. Huang and Y.-L. Huang, “Effect of multi-layered induction coils on efficiency and uniformity of surface heating,” *International Journal of Heat and Mass Transfer*, vol. 53, no. 11-12, pp. 2414–2423, May 2010.
- [64] S. Kirkpatrick, “Optimization by simulated annealing,” *Science*, 1983.
- [65] K. Deb, A. Pratap, S. Agarwal, and T. Meyarivan, “A fast and elitist multiobjective genetic algorithm: NSGA-II,” *IEEE Transactions on Evolutionary Computation*, vol. 6, no. 2, pp. 182–197, Apr. 2002.
- [66] V. Rudnev, “Handbook of induction heating,” 2003.
- [67] J. A. Nelder and R. Mead, “A Simplex Method for Function Minimization,” *The Computer Journal*, vol. 7, no. 4, pp. 308–313, Jan. 1965.
- [68] R. Marler and J. Arora, “Survey of multi-objective optimization methods for engineering,” *Structural and Multidisciplinary Optimization*, vol. 26, no. 6, pp. 369–395, Apr. 2004.
- [69] E. Zitzler and L. Thiele, “Multiobjective evolutionary algorithms: a comparative case study and the strength Pareto approach,” *IEEE Transactions on Evolutionary Computation*, vol. 3, no. 4, pp. 257–271, 1999.
- [70] J. Phillips and J. White, “Precorrected-FFT methods for electromagnetic analysis of complex 3-D interconnect and packages,” in *Progress Electromagn. Res. Symp*, vol. 95, 1995.
- [71] D. Wolpert and W. Macready, “No free lunch theorems for optimization,” *IEEE Transactions on Evolutionary Computation*, vol. 1, no. 1, pp. 67–82, Apr. 1997.